



Solvent-exposed lipid tail protrusions depend on lipid membrane composition and curvature



Mukarram A. Tahir¹, Reid C. Van Lehn¹, S.H. Choi, Alfredo Alexander-Katz*

Department of Materials Science and Engineering, Massachusetts Institute of Technology, Cambridge, MA, USA

ARTICLE INFO

Article history:

Received 22 June 2015

Received in revised form 20 January 2016

Accepted 27 January 2016

Available online 30 January 2016

Keywords:

Membrane fusion

Molecular dynamics

Lipid splay

Lipid backfolding

Stalk

Pre-stalk

Hydrophobic contact

ABSTRACT

The stochastic protrusion of hydrophobic lipid tails into solution, a subclass of hydrophobic membrane defects, has recently been shown to be a critical step in a number of biological processes like membrane fusion. Understanding the factors that govern the appearance of lipid tail protrusions is critical for identifying membrane features that affect the rate of fusion or other processes that depend on contact with solvent-exposed lipid tails. In this work, we utilize atomistic molecular dynamics simulations to characterize the likelihood of tail protrusions in phosphatidylcholine lipid bilayers of varying composition, curvature, and hydration. We distinguish two protrusion modes corresponding to atoms near the end of the lipid tail or near the glycerol group. Through potential of mean force calculations, we demonstrate that the thermodynamic cost for inducing a protrusion depends on tail saturation but is insensitive to other bilayer structural properties or hydration above a threshold value. Similarly, highly curved vesicles or micelles increase both the overall frequency of lipid tail protrusions as well as the preference for splay protrusions, both of which play an important role in driving membrane fusion. In multi-component bilayers, however, the incidence of protrusion events does not clearly depend on the mismatch between tail length or tail saturation of the constituent lipids. Together, these results provide significant physical insight into how system components might affect the appearance of protrusions in biological membranes, and help explain the roles of composition or curvature-modifying proteins in membrane fusion.

© 2016 Elsevier B.V. All rights reserved.

1. Introduction

Phospholipids are biological amphiphiles consisting of two hydrophobic tails and a hydrophilic head group that self-assemble into a characteristic bilayer structure in water. The lipid bilayer is one of the primary components of the cell membrane and is critical for regulating transport into and out of the cell. For example, the low dielectric constant of the hydrophobic tail region minimizes the passive diffusion of water, ions, and other small hydrophilic molecules through the membrane [1]. As a result, water-soluble molecules are often encapsulated within lipid vesicles to facilitate intra- and extracellular trafficking. The exchange of molecules between such vesicles, or between vesicles and other lipid-bound compartments, occurs after membrane fusion. In this process, two lipid bilayers merge to form a single connected structure that allows the mixing of contents from the previously distinct compartments. Fusion between lipid vesicles is one of the primary mechanisms for the transport of hydrophilic small molecules, lipids, or proteins throughout the cell; for example, endosomes containing internalized material will fuse with endosomal sorting complexes as part of a recycling pathway [2]. Similarly, fusion between internal vesicles and

the outer membrane triggers the secretion of soluble proteins to the extracellular environment during exocytosis and is necessary for the transport of neurotransmitters at synapses [3,4]. These biological fusion processes are generally accelerated by membrane-bound SNARE proteins from opposing membranes forming a supramolecular complex that facilitates membrane proximity and enables lipid mixing to drive stalk formation and membrane fusion [5,6].

Given the biological relevance of membrane fusion, there has been significant work aimed at understanding its physical mechanism. The generally accepted fusion pathway involves three intermediate states with corresponding energy barriers [7–9]. First, two bilayers must approach within a distance of approximately 0.9 nm¹⁰, which requires overcoming a repulsive hydration force associated with dehydrating the intervening solvent region, [10–12]. Next, contact between hydrophobic lipid tails in the two apposed bilayers nucleates the formation of a lipid stalk, or a highly curved lipid bridge formed from the mixture of the two proximal lipid monolayers [13,14]. The stalk then radially expands into a hemifusion intermediate to reduce the bending energy of the disrupted lipids [7,15]. Finally, full fusion occurs if the hemifusion intermediate ruptures and forms an aqueous channel through the two bilayers that allows for the transfer of contents [16,17]. Experimental approaches have been valuable in characterizing several of these transitions, including the magnitude of the repulsive hydration force [10,11], barrier to lipid mixing [15], and expansion of the stalk [16,18]. However,

* Corresponding author.

E-mail address: aalexand@mit.edu (A. Alexander-Katz).

¹ These authors contributed equally to this work.

detailed molecular insight into the nature of these transitions is difficult to assay experimentally but is necessary to understand the role of various components in the fusion pathway, such as fusion proteins [19] or different lipid compositions [10,20].

Recently, computer simulations have become increasingly valuable in understanding the mechanism of fusion by providing this missing molecular detail [9,21–30]. In particular, particle-based molecular simulations are capable of resolving the lipid mixing that marks the onset of stalk formation. Multiple different simulation methodologies have led to the identification of a pre-stalk transition involving the stochastic protrusion of hydrophobic lipid tails into the solvent layer between two vesicles [23,31–35]. Contact between protruding lipid tails has been established as a transition state prior to stalk formation; if such contact occurs, the pre-stalk intermediate may relax to a metastable stalk [32,33,36]. As a result, it is critical to understand the conditions under which tail protrusions are promoted in order to identify membrane components that encourage the pre-stalk transition. Moreover, similar lipid tail protrusions have been shown to trigger the spontaneous insertion of amphiphilic nanoparticles into lipid bilayers [37], raising the possibility that these stochastic fluctuations may be important in other processes involving contact between hydrophobic molecules and the bilayer core. Molecular dynamics simulations and neutron diffraction experiments have provided direct evidence for the incidence of these protrusions, with a substantial concentration of acyl-chain methyl groups observed to intercalate with lipid head groups and access interfacial solvent molecules in phospholipid bilayers [38]. In addition, recent simulations have examined related lipid fluctuations, such as the formation of hydrophobic defects [39–41] or lipid desorption [42, 43]. To the best of our knowledge, however, no substantial study has yet been performed to systematically investigate the factors that influence the likelihood of lipid tail protrusions in protein-free bilayers.

In this work, we use atomistic molecular dynamics simulations to quantify the likelihood of observing the spontaneous protrusion of a single lipid tail into aqueous solution. We further use umbrella sampling simulations to calculate the potential of mean force (PMF) required to induce a protrusion, then compare PMFs for several different lipid compositions. The PMFs show that the free energy cost for a protrusion depends on lipid tail saturation and the location of the protruding lipid tail atom but is insensitive to tail length in lipids with phosphatidylcholine head groups. The preference of atoms near the head group or near the tail end to protrude leads to the classification of both “elbow” and “splay” protrusion modes, respectively. Moreover, we find a significant increase in the PMF below a critical level of bilayer hydration corresponding to the interpenetration of lipid head groups. To supplement these free energy calculations, we calculate the protrusion likelihood from unbiased simulations of bilayers with different compositions, curvature, and hydration. We find that protrusions occur on an approximately 100 ns timescale depending on the extent of solvent exposure. Crucially, we observe that bilayer curvature can substantially increase the incidence of these protrusion events relative to planar bilayers. This work shines significant physical insight into the likelihood of observing spontaneous protrusions in planar and curved homogeneous bilayers and how membrane features like composition, curvature, and hydration can affect protrusion propensity, which has applications in understanding and potentially manipulating this barrier in processes of biological interest.

2. Methods

Atomistic molecular dynamics simulations were used to model a series of lipid bilayers to quantify protrusion likelihood. Five different single-component lipid bilayers—containing DLPC, DMPC, DPPC, POPC, or DOPC—were constructed by extracting 64 lipids from the 128 lipid pre-equilibrated bilayers provided by Poger et al. [44]. All five lipid species have zwitterionic phosphatidylcholine head groups but differ in the number and saturation of carbon atoms in the tail groups (chemical

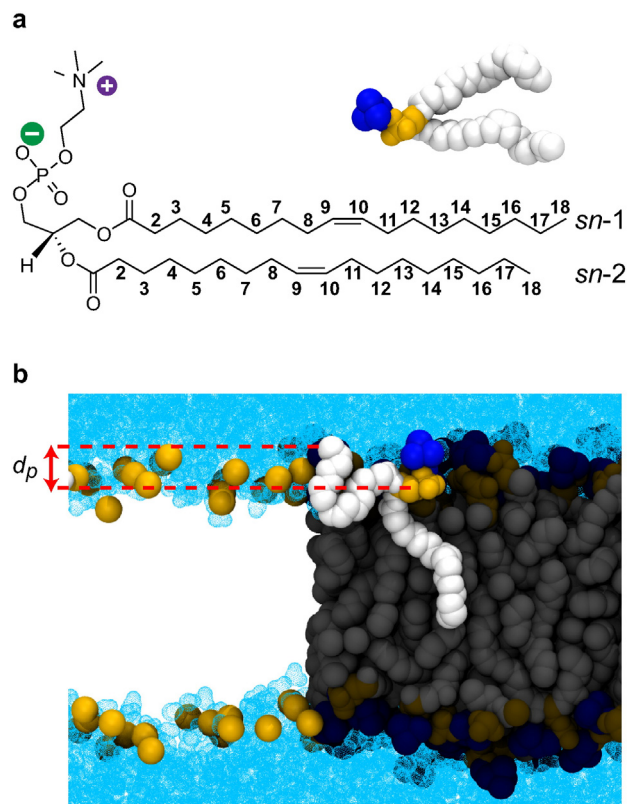


Fig. 1. Lipid structure and protrusion definition. **a** Chemical structure of DOPC and simulation representation. Atom indices in both tails are numbered starting from the glycerol group. **b** Example protrusion and definition of d_p , the distance between a hydrophobic tail atom and the same lipid's phosphorus atom projected along the membrane normal. Several additional phosphorus atoms are shown to illustrate that they are roughly coplanar in the bilayer. Lipid tails are in white, the phosphate group in yellow, the choline group in blue, and water in cyan. All images were generated using Visual Molecular Dynamics [52].

structures shown in Fig. 1 and Fig. S1). The 64 lipids were resolvated to have 50–60 water molecules per lipid. One bilayer, composed of DOPC, was simulated at both 300 K and 323 K. All other bilayers were run at 323 K, a temperature well above the gel-fluid phase transition (Table S1). We also investigated the effect of bilayer hydration, curvature, and inhomogeneity on the likelihood of lipid tail protrusion. 64 lipid DOPC bilayers were prepared with 5, 7, 10, 25, and 60 water molecules per lipid to vary the water layer thickness and simulated at 300 K. Bilayers constructed with a binary mixture of lipids that differed in either tail length (DPPC/DLPC) or tail saturation (DPPC/DOPC) were prepared through a reverse coarse-graining procedure [45] using the MARTINI force field [46] as described in the Supplementary Information (Fig. S2). Each mixed bilayer contained 512 lipids in a 1:1 ratio of the two components, with the larger bilayer size permitting suitable lipid interdiffusion, and was simulated at 323 K. Finally, a 50 lipid DOPC micelle and a 900 lipid DOPC vesicle were both constructed using a similar reverse coarse-graining procedure (Fig. S2). Physical properties of all systems simulated are summarized in Table S1.

All systems were modeled using the GROMOS 54a7 force field with the SPC water model [44,47,48]. A leap-frog molecular dynamics integrator was used with a timestep of 2 fs. System configurations were saved every 20 ps. All bonds were constrained using the LINCS algorithm [49]. Long-range electrostatic interactions were modeled using the smooth particle mesh Ewald (PME) method with a grid spacing of 0.12 nm and fourth-order interpolation. The neighbor list cutoff, van der Waals cutoff, and short-range electrostatics cutoff were all set to 1.0 nm to match recent simulation methods [50]. Constant temperature was maintained at either 300 K or 323 K using a velocity-rescale thermostat with a timestep of 0.1 ps. Constant pressure was maintained at

1 bar using either a Berendsen or Parrinello-Rahman barostat. Semiisotropic pressure coupling was used to decouple box motion in the x/y and z dimensions for planar bilayers while isotropic pressure coupling was used for the spherically symmetric micelle and vesicle systems. For both barostats, a 1.0 ps time constant was used and the isothermal compressibility was set to $4.5 \times 10^{-5} \text{ bar}^{-1}$. Most simulations were first equilibrated for 20 ns using the Berendsen barostat then an additional 100 ns using the Parrinello-Rahman barostat. The dehydrated systems were equilibrated for an additional 100 ns using a Parrinello-Rahman barostat due to the observation of a slow drift in the area per lipid after 100 ns. Shorter equilibration times were used for the micelle and vesicle due to the previous long equilibration using the MARTINI force field (see Supplemental Information). Simulations were repeated at least once from distinct initial velocities. All simulation parameters are summarized in Table S2. Simulations were performed using Gromacs version 4.6.1 [51].

Lipid protrusions were identified in the unbiased simulations by calculating the distance between a hydrophobic atom in a lipid tail and the same lipid's phosphorus atom. This distance was then projected along the membrane normal (i.e. the z-axis) and defined as d_p . If d_p exceeded a threshold value for any tail atom the lipid was recorded as a protrusion. The same definition has been used previously in determining the likelihood of vesicle fusion [33,34]. Fig. 1 depicts the chemical structure and simulation representation of a typical lipid, DOPC, as well as the definition of d_p for an example protrusion. For the curved micelle and vesicle, the membrane normal was calculated for each lipid as the vector from the head group phosphorus atom to the center of mass of all solvent molecules within 1.5 nm. d_p was then redefined as the distance between a lipid tail atom and the nearest lipid's phosphorus atom, projected along the locally-varying membrane normal. Additional details are in the Supplemental Information and Fig. S3.

The potential of mean force (PMF) for a lipid protrusion was calculated from umbrella sampling simulations using the Weighted Histogram Analysis Method (WHAM) [53,54]. The reaction coordinate for umbrella sampling was defined as the distance from the center of mass (COM) of the bilayer along the membrane normal. Umbrella sampling windows were spaced by 0.1 nm with the number of windows determined from the thickness of the bilayer (Table S2). For each window, a single united atom bead was first pulled for 2 ns to the desired distance from the bilayer COM using a harmonic potential with a spring constant of 500 kJ/mol/nm². The spring constant was then increased to 3000 kJ/mol/nm² to restrain the atom for another 2 ns of equilibration before 70 ns of umbrella sampling were performed with the same spring constant. All atoms of the lipid being restrained were excluded from the bilayer COM calculation. For systems with a single bilayer, two lipid protrusions were induced simultaneously to reduce computational expense as shown in Fig. S4 [42]. For the DOPC bilayers with varying levels of hydration, a double bilayer system was created by duplicating two equilibrated bilayers with the desired level of hydration along the z-axis. A single lipid was then restrained in umbrella sampling as shown in Fig. S5. The PMF was calculated using the program *g_wham* with 201 bins [55]. All plots in the results show two independent PMF curves with the minimum set to 0. The convergence of a typical PMF plot within 70 ns is shown in Fig. S6.

3. Results

3.1. Protrusion likelihood from unbiased simulations

As a first examination of protrusion likelihood, Fig. 2 shows the time-averaged number of protrusions per lipid determined from 200 ns unbiased simulations of 64-lipid bilayers. Protrusion likelihood from two samples each is reported for all five single-component bilayer compositions and for both DOPC temperatures to test the effect of lipid structural properties. While the protrusion likelihood increases slightly with increased system size (as shown in Fig. 9) due to stronger bending

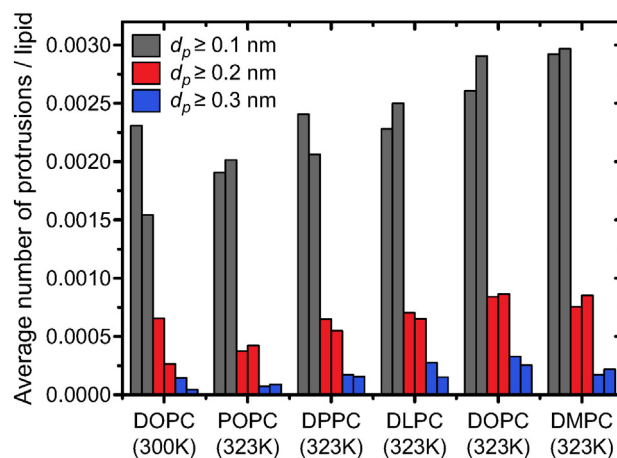


Fig. 2. Average number of protrusions per lipid for five bilayer compositions, including two temperatures for DOPC, time-averaged over 200 ns and shown for three different values of the threshold d_p .

undulations in larger bilayers, we compare protrusion likelihood between bilayers containing 64 lipids to maintain consistency with the PMF calculations and to focus on differences in protrusion frequency as a function of lipid composition. Three threshold values of d_p were considered: 0.1 nm, 0.2 nm, and 0.3 nm. All three values are in excess of the threshold previously used to show a correlation between tail protrusions and successful vesicle fusion [34]. The results indicate that tail protrusions are rare events for all bilayer compositions, with only approximately 1 in 500 lipids protruding for any given system snapshot for the $d_p \geq 0.1 \text{ nm}$ threshold. The total protrusion propensity diminishes significantly with an increase in d_p with only 1 in 5000 lipids protruding for the threshold of $d_p \geq 0.3 \text{ nm}$. While the increase in observed protrusions between the DOPC bilayer at 300 K and 323 K can be attributed to the increase in attempt probability or additional thermal energy available at the elevated temperature, changes in protrusion likelihood between different lipids did not correlate with properties such as bilayer thickness, area per lipid, or tail length (c.f. Table S1). As the difference in protrusion probability was within 50% for all lipids studied, it is possible that the differences reflect sampling limitations due to the infrequent observation of protrusions. We can therefore conclude that protrusion probability is unaffected by lipid type in bilayers composed of lipids with phosphatidylcholine head groups.

A next question is whether particular tail atoms preferentially protrude. Fig. 3 shows the fraction of total protruding atoms for each bead in the DOPC tails measured from the simulations at 300 K using a threshold of $d_p \geq 0.1 \text{ nm}$. Each tail atom is numbered according to the legend in Fig. 1a. The results indicate a clear preference for two protrusion modes that we classified as “elbow” or “splay” depending on whether the protruding atom was located near the lipid head group or end of the tail respectively. Example snapshots of each are shown in Fig. 3. Elbow protrusions were more common than splay for all lipid types as shown in Fig. S7. Previous simulations of vesicle-vesicle fusion have shown that both protrusion modes can initiate stalk formation. For example, a single splay protrusion may span the solvent layer between apposed vesicles [31,32,36], or two protrusions may contact each other in the intervening solvent layer. Simulation snapshots from Mirjanian et al. (Fig. 7 in Ref. 30) and Kasson et al. (Fig. 4 in Ref. 31) also illustrate pre-stalk intermediates involving elbow protrusion contact. The shallow elbow protrusions may also be similar to the hydrophobic defects reported by Vanni and co-workers as related to peripheral protein binding [39–40,56]. Finally, both types of protrusions have been observed to trigger the insertion of nanoparticles into bilayers through the edge of bilayer defects [37], indicating their importance in processes other than vesicle fusion.

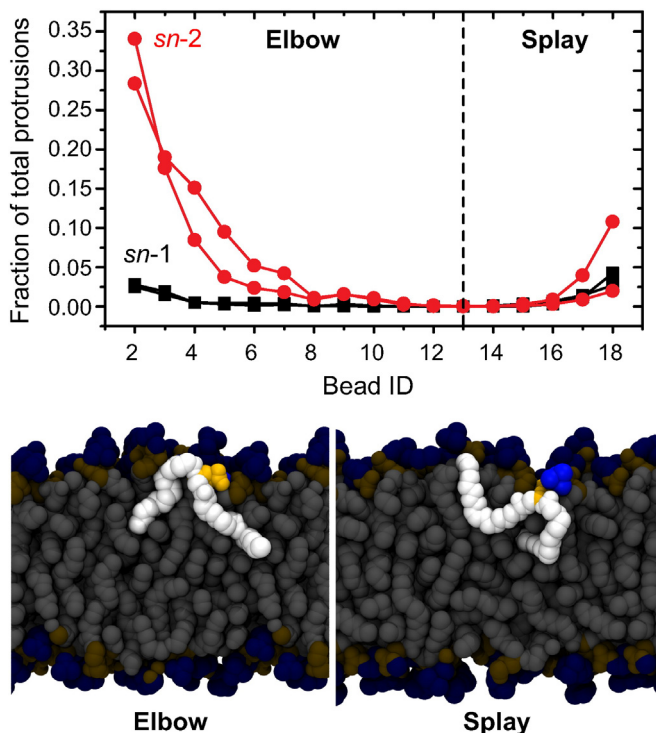


Fig. 3. Relative fraction of total protruding atoms for each hydrophobic bead in lipid tail. Protrusions were identified as beads with $d_p \geq 0.1$ nm with the definition of d_p and bead IDs shown in Fig. 1. Two types of tail protrusions were identified: “elbow” protrusions, involving beads close to the lipid head group, and “splay” protrusions, involving beads near the end of the tails. An example of each protrusion type is shown with the protruding lipid highlighted.

The previous unbiased results report protrusion likelihood as a time-averaged number of protrusions per lipid. Fig. S8 alternatively reports the number of protrusions per lipid per nanosecond as a measure of protrusion frequency. Only unique events were counted by disregarding protruding tails that were also protruding in the previous simulation snapshot. Elbow protrusions occurred over a timescale of approximately 10–100 ns per lipid depending on the value of d_p while splay

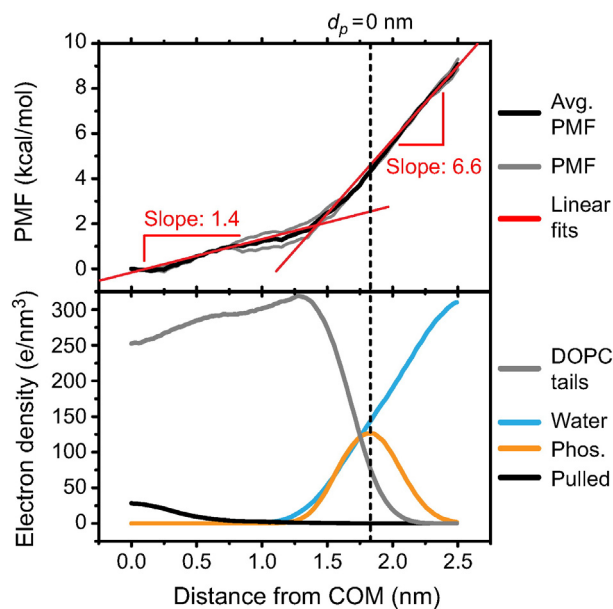


Fig. 4. Potential of mean force (PMF) for a splay protrusion in a DOPC bilayer at 300 K, paired with electron density profiles of water, lipid tail atoms, and phosphate atoms in the unperturbed system. The dashed vertical line corresponds to $d_p = 0$ nm.

protrusions were observed on a timescale of approximately 100–1000 ns. The overall trends in protrusion frequency mirrored the measurements in Fig. 4. Given that stalk formation requires either a single splay protrusion to extend across the entire solvent region or multiple protrusions contacting within the solvent region, the relatively long timescales for these processes explain why planar bilayers, or a vesicle and a planar bilayer, have not been shown to fuse within simulation timescales without perturbing the system [32,36].

3.2. Protrusion potential of mean force

To complement the unbiased simulations, the potential of mean force (PMF) for generating a protrusion was calculated for the same set of lipid compositions. Note that we utilized 64-lipid bilayers here due to the high computational expense of calculating the PMFs for lipid protrusions. As previously mentioned, the effective likelihood of protrusion is slightly decreased as system size is reduced, mainly due to finite size effects such as the suppression of bilayer undulations. The PMFs computed here can therefore be interpreted as an upper bound on the barrier for lipid tail protrusion into solvent. Fig. 4 shows the PMF for a splay protrusion in a DOPC bilayer at 300 K calculated by restraining the last atom of the *sn-1* lipid tail. Electron densities of water, the hydrophobic lipid tails, and phosphate atoms in the system are also plotted on the same axes as the PMF. The dashed line corresponds to the location of peak phosphate density where $d_p = 0$ as defined previously. The PMF profile demonstrates two approximately linear regimes with distinct slopes that can be identified by comparison with the electron density plots. In the initial, low-slope regime, the protrusion is coordinated by an increasing density of lipid tail groups, indicating largely a steric/entropic barrier. The point where the slope of the PMF changes coincides with an increase in water density that tracks the PMF. The exposure of the hydrophobic lipid tail to water leads to a large barrier. Fig. S9 shows coordination numbers for the protruding lipid to confirm that the electron densities reflect the distribution of components around the protruding tail.

From the PMF, the free energy cost for inducing protrusions to the phosphate peak is approximately 5 kcal/mol, or 8.4 kT at 300 K, and the barrier grows with a slope of 6.6 kcal/mol/nm. Assuming that the change in protrusion likelihood is proportional to $e^{-\Delta F/kT}$, where ΔF is the change in the PMF, the calculated slope predicts a decrease in protrusion probability by a factor of 0.33 of a 0.1 nm change in d_p . Indeed, this change is approximately what is observed for different d_p thresholds in the unbiased results in Fig. 2, indicating that the change in protrusion likelihood can be attributed to the thermodynamic cost captured in the PMF. The magnitude of the PMF is also similar to previous estimates for protrusions induced prior to vesicle fusion. For example, Smirnova et al. estimated the cost for a single splay protrusion as 14 kT and the barrier for two splay protrusions making contact as 18–20 kT [36], Muller et al. estimated the barrier for the pre-stalk transition as 16.3 kT [28], and Mirjanian et al. found a larger barrier of approximately 13–22 kT depending on lipid composition, although this value included the cost for dehydrating the vesicle-vesicle interface [32]. It should also be noted that all of these previous estimates use coarse-grained models, unlike the atomistic model employed here, that may less accurately account for contributions to the PMF associated with lipid degrees of freedom. The measured PMF thus confirms the trends identified in Fig. 2, compares reasonably to other simulation findings, and suggests that changes in protrusion likelihood can be mapped directly to protrusion thermodynamics.

Next, PMFs for pulling on various beads in the *sn-1* tail of a DOPC lipid were calculated at 300 K. Fig. 5 shows PMFs for the different atoms labeled in the DOPC chemical structure. The barrier for protrusion is lower for beads near the end of the lipid tail (black lines) and near the glycerol group (green lines), corresponding to the observed preference for splay and elbow protrusions respectively (Fig. 3). Likewise, the free energy barrier for protrusion of the middle beads (red and blue lines)

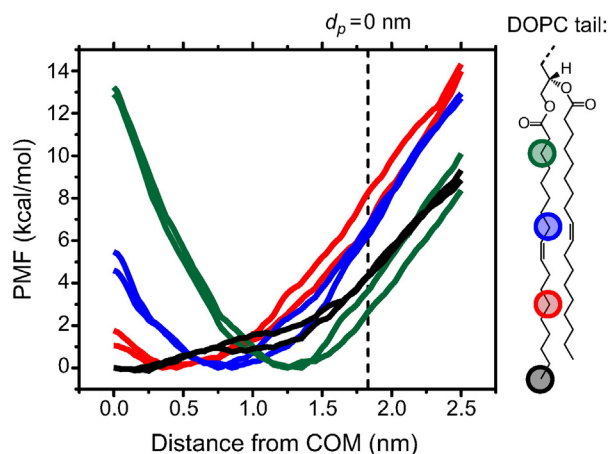


Fig. 5. PMFs for pulling different *sn*-1 lipid tail atoms in a DOPC bilayer at 300 K. Curves are colored to correspond to the atoms labeled in the DOPC tail structure drawn on the right. The dashed vertical line indicates where $d_p = 0$ nm.

is significantly higher, which is consistent with the near-zero protrusion probability of the middle beads in Fig. 3. Pulling on atoms near the middle of the tail induces the exposure of adjacent atoms to solvent, unlike elbow or splay protrusions near the chain ends (see snapshots in Fig. 3). This behavior explains the higher PMF for the middle atoms and the minimal probability of observing such protrusions in unbiased simulations. There is a small difference in the barrier for inducing a splay or elbow protrusion to $d_p = 0$ which may partially explain the higher frequency of elbow protrusions (Fig. 3), although this may also be due to the proximity of the elbow atoms to the solvent interface that allows more frequent protrusion attempts. The slope of the splay PMF is also lower than that of the elbow PMF as the tail enters the solvent region, suggesting a potential shift toward a higher relative frequency of splay protrusions for larger values of d_p .

To compare the free energy barrier for protrusions in lipids of varying tail length and saturation, the PMF for inducing a splay protrusion was computed for DLPC, DMPC, DPPC, DOPC, and both tails of POPC at 323 K. To compare bilayers with different thicknesses (c.f. Table S1), the reaction coordinate is expressed as the distance from the maximum of the phosphate peak, a measure effectively equivalent to d_p . Fig. 6a shows that all three saturated lipids have nearly identical PMFs despite different tail lengths. Fig. 6b compares the unsaturated tail of POPC with the unsaturated lipid of identical tail length, DOPC, and compares the saturated tail with the equivalent lipid DPPC. The PMFs between the saturated and unsaturated tails of POPC are nearly identical to the corresponding DOPC and DPPC PMFs, indicating that the PMF only depends on the degree of tail saturation and not on the complete bilayer structure. Moreover, the PMFs between the unsaturated and saturated tails only differ in a plateau region where the distance to the phosphate peak is approximately -1.0 to -0.5 nm. The slight decrease in the PMF in this region may be attributed to the “kink” caused by the *cis* conformation of the double bond in the unsaturated tail. While the overall magnitude of the barrier does not decrease significantly, and as a result does not appear to correlate with the unbiased probability likelihood (Fig. 2), the observed effect of a single double bond suggests that polyunsaturated lipids may exhibit much higher protrusion frequencies. Previous experimental measurements have shown that acyl chains in polyunsaturated lipids do reside closer to the head group-solvent interface, supporting this possibility [57].

3.3. Effect of bilayer hydration

Prior to stalk formation, two bilayers must come into close proximity by dehydrating the local interface [12]. This dehydration may potentially impact the protrusion of lipid tails into the thinned intervening

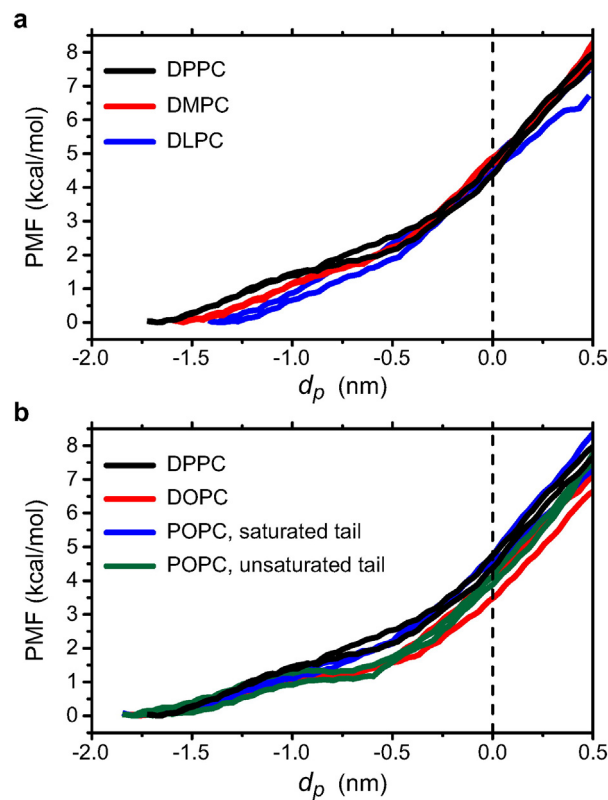


Fig. 6. PMFs for splay protrusions in bilayers of varying compositions. **a** Comparison of PMFs for three saturated lipids with different tail lengths. **b** Comparison of saturated DPPC and unsaturated DOPC lipids with both tails of asymmetric lipid POPC.

solvent layer. PMFs were computed for DOPC double bilayers at 300 K with 5, 7, 10, 25, and 60 water molecules per lipid corresponding to water layer thicknesses (D_w) of 0.6 nm, 0.8 nm, 1.1 nm, 2.5 nm, and 5.7 nm respectively. The water layer thickness was estimated from the distance between phosphate peaks in electron density profiles of the dehydrated bilayers as discussed in the Supplemental Information and Fig. S5. Fig. 7 shows that the PMF is relatively unaffected for hydration levels as low as 7 water molecules per lipid ($D_w = 0.8$ nm). For a hydration of 5 water molecules per lipid ($D_w = 0.6$ nm) there is a large increase in the PMF leading to a significantly higher protrusion barrier.

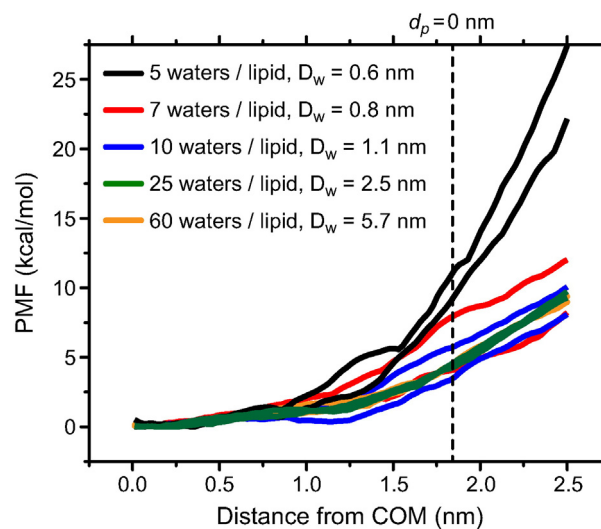


Fig. 7. PMF for a splay protrusion in DOPC bilayers subject to different levels of hydration, measured both by the number of water molecules per lipid and the thickness of the intervening solvent region (D_w).

Unbiased calculations also show a drop in the average number of protrusions for only this level of hydration (Fig. S8f). At this water layer thickness, there is substantial interpenetration between head groups in the apposed bilayers as shown by the electron density plots in Fig. S5 and observed in previous simulations [58,59]. The enhanced head group density could act as a steric barrier to protrusions, explaining the PMF increase. Moreover, a recent study of the dynamics of lipids and water under the same dehydrated conditions has shown that the lipids in both apposed bilayers co-diffuse and exhibit slowed, glassy dynamics [60]. Given this coupling and the necessity of rearranging nearby lipids to access the aqueous interface, the low-hydration PMF may include contributions for deforming both bilayers in the double bilayer system.

The hydration PMFs suggest that there is an optimal inter-bilayer separation at which lipid protrusions are most likely and hence stalk formation should be preferred. The results indicate that protrusion contact would be most probable when two bilayers approach to within a distance of approximately 0.8 nm (7 water molecules/lipid) in order to minimize the distance to which protrusions need to extend but without incurring the additional free energy cost associated with lower hydrations (i.e. 5 water molecules/lipid). In recent experimental work, Aeffner et al. found that the critical distance for spontaneous stalk formation was measured as approximately 0.9 nm independent of lipid composition [10]. Moreover, after stalk formation, the water layer thickness suddenly increased for most bilayers, suggesting that the critical distance may not be set by the stability of the stalk. This distance corresponds to a hydration level in between 7 and 10 water molecules/lipid based on our measurements, where the PMF for inducing a protrusion is identical to the bulk values as shown in Fig. 7. The authors also suggested that 0.9 nm is a critical distance at which splay protrusions can come into contact as a pre-stalk intermediate. Our results support this hypothesis by showing that 0.9 nm is approximately the closest separation that bilayers can approach before the cost for protrusions dramatically increases, implying that the pre-stalk transition should occur near this distance before relaxing into a stable stalk. Moreover, the independence of the 0.9 nm critical distance on lipid composition agrees with the similarity of the PMFs shown in Fig. 6 for several different bilayer compositions.

3.4. Protrusion likelihood in curved and mixed bilayers

An important factor that may affect protrusion likelihood is bilayer curvature. In previous simulations, low-curvature planar single-component bilayers were not observed to spontaneously fuse [32,36], while high curvature vesicles could fuse within short simulation time-scales [32,33]. This observation was commensurate with experimental investigations of lipid vesicles with re-constituted SNARE proteins, where vesicle fusion efficiency and size of the supramolecular SNARE complex was proportional to membrane curvature [6]. High membrane curvature is associated with a number of effects, such as lateral membrane stresses, which may explain this enhanced likelihood of fusion. We hypothesize that membrane curvature may additionally increase the likelihood of solvent-exposed lipid tail protrusions. As previously discussed, these protrusions have been shown to play an essential part in driving membrane fusion [32,33,36], so understanding the relationship between membrane curvature and protrusion likelihood may provide additional insights into the role of curvature in driving membrane fusion.

To test this effect, a small DOPC vesicle (13.2 nm in diameter) and micelle (5.0 nm in diameter) were compared to a planar DOPC bilayer. The micelle represents an effective extreme of curvature due to its small diameter, and is hence utilized here to investigate how the presence of large curvature affects the likelihood of lipid tail protrusions. Snapshots of the different systems are illustrated in Fig. 8a. Fig. 8b shows the average number of protrusions per lipid for these three structures for different threshold values of d_p . The protrusion likelihoods

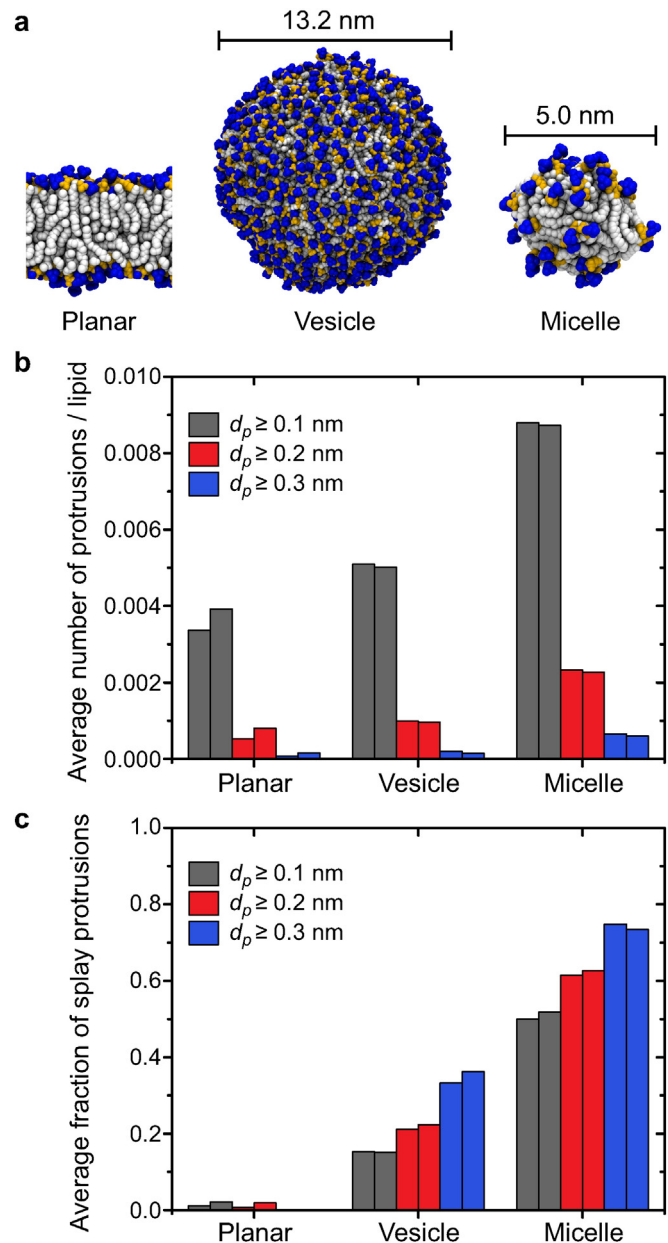


Fig. 8. Effect of curvature on protrusion likelihood. **a** Snapshots of three systems of increasing curvature. **b** Average number of protrusions for different threshold values of d_p as a function of curvature. **c** Average fraction of splay protrusions for different threshold values of d_p as a function of curvature.

reported for the planar bilayer are slightly different than those reported in Fig. 2 because they are calculated using a slightly different algorithm developed for the curved bilayers as discussed in the Methods and Supplemental Information (Fig. S3). The trends in protrusion likelihood as a function of d_p are preserved, however.

Fig. 8b shows a large increase in the average number of protrusions as the curvature increases, with the micelle exhibiting a $2.4\times$ increase in protrusions relative to the planar bilayer for $d_p \geq 0.1$ nm and $5.3\times$ increase for $d_p \geq 0.3$ nm. More modest increases of $1.39\times/1.48\times$ for $d_p = 0.1/0.3$ nm were observed for the vesicle. These results agree with the previous finding of lipid tail “backfolding” in the outer leaflet of lipid vesicles where the separation of head groups induced by the curvature causes lipid tails to access free volume in the head group region [61]. This behavior also leads to an increase in the relative proportion of splay protrusions as shown in Fig. 8c, with splay becoming the dominant protrusion mode for the small micelle. The proportion of splay

protrusions also increases with d_p , agreeing with the PMF in Fig. 5 which shows a lower slope for splay as opposed to elbow protrusions, an effect magnified in the curved bilayers. Given this shift in the relative frequency of splay protrusions, the likelihood of observing a splay protrusion increases by a factor of 13.2 for the vesicle and 76.5 for the micelle for $d_p \geq 0.1$ nm. This large increase in splay protrusion frequency with curvature explains why simulations of small vesicles lead to the observation of spontaneous fusion, especially given that a single splay protrusion may be sufficient to drive stalk formation [36].

It is important to note that unlike the single-component bilayers considered so far, biological membranes are complex assemblies of multiple lipid species and other molecules [62] that may exhibit distinct protrusion propensities. For example, prior simulations have shown that membrane-active fusion peptides may promote lipid tail protrusions by locally disordering lipid tails [34], with a similar increase observed in the vicinity of membrane-embedded nanoparticles [63]. To assess whether a similar increase in protrusion incidence would emerge in bilayers that are assembled from a mixture of phosphatidylcholine lipids, we constructed bilayers from binary mixtures of lipids differing either in tail length (DPPC/DLPC) or tail saturation (DPPC/DOPC) and calculated the average number of protrusions per lipid from unbiased simulations. Lipid interdiffusion was achieved by initially simulating for 3 μ s with a coarse-grained force field prior to reverse coarse-graining the system back to atomistic resolution as detailed in the Supplemental Information. A system size of 512 lipids was necessary for simulating the mixed bilayers in order to properly capture lipid interdiffusion. To compare mixed bilayer protrusion frequencies with single-component ones, we re-calculated DOPC, DLPC, and DPPC protrusion frequencies from 512-lipid single-component bilayers in order to rule out system size effects.

Fig. 9 compares the likelihood of lipid tail protrusions in DPPC/DLPC and DPPC/DOPC mixed bilayers with single-component DPPC, DLPC, and DOPC bilayers at 323 K. Protrusion frequencies calculated from single-component 64-lipid simulations are also shown for reference. Simulation snapshots illustrate the extent of lipid mixing. We observe minimal difference in the likelihood of protrusion between mixed bilayers and single-component ones, as calculated from 512-lipid systems. Through additional analysis, we also find that the nature of the surrounding lipids, specifically the six nearest neighbors, does not alter the propensity of forming protrusions in the mixed bilayers (data not shown). We can therefore conclude that protrusion likelihood is not enhanced in bilayers that are assembled from binary mixtures of phosphatidylcholine lipids that differ in either tail length or tail saturation. Comparing the protrusion frequency for each lipid type in Fig. 9 between the 64-lipid and 512-lipid bilayers also reveals that system size does affect protrusion likelihood, as the single-component protrusion frequencies calculated from the 512-lipid bilayers are greater than those calculated from 64-lipid bilayers. In visualizing simulation trajectories, as shown in the included Supplementary Video for DLPC bilayers, we observe more pronounced bending undulations in the 512-lipid bilayers compared to the 64-lipid ones. These bending undulations are associated with higher membrane curvature, so the increase in protrusion frequency with system size additionally supports the hypothesis that the presence of membrane curvature increases the likelihood of lipid tail protrusions.

4. Discussion

Using atomistic molecular dynamics simulations, we quantified the likelihood of observing protruding solvent-exposed lipid tails in lipid bilayers as a function of bilayer composition, hydration, and curvature. Unbiased simulations of 5 different zwitterionic lipid compositions varying in tail saturation and length showed that on average only 0.2–0.3% of lipids protrude into solvent for any given simulation snapshot when protrusions were identified with the lowest threshold value of $d_p = 0.1$ nm. This value fell by an order of magnitude if the threshold

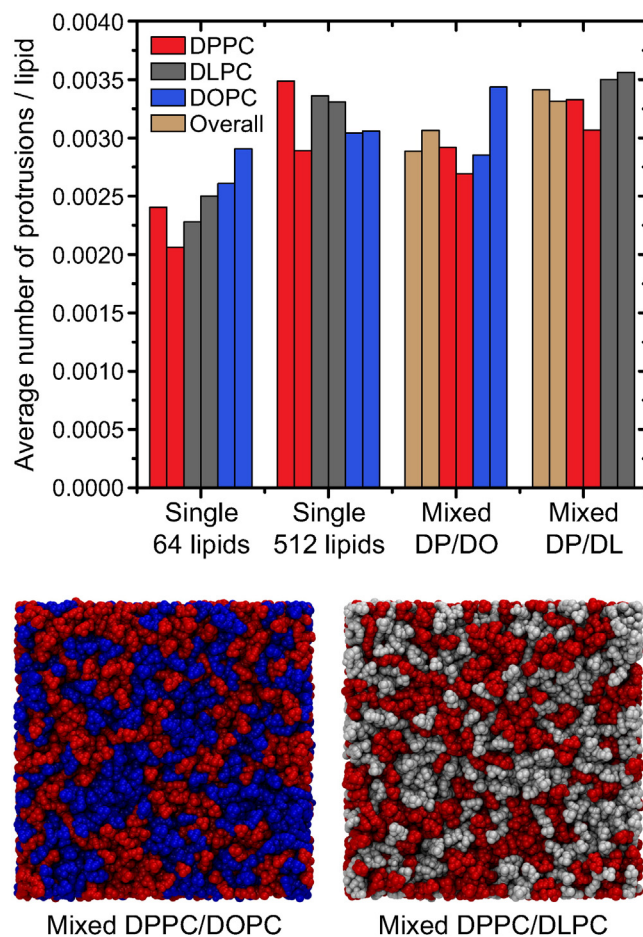


Fig. 9. Average number of tail protrusions in 512-lipid bilayers composed of a binary mixture of lipids that differ in thickness (DPPC/DLPC) or tail saturation (DPPC/DOPC), compared with corresponding single-component bilayers. Single-component protrusion frequencies calculated from 64-lipid bilayers are also shown for reference. The simulation snapshots show views of the bilayers along the z-axis to show lipid mixing.

was increased to $d_p = 0.3$ nm. Two protrusion modes were identified, with most protrusions in planar bilayers characterized as “elbow” protrusions where hydrophobic atoms near the lipid head group entered solvent. In contrast, “splay” protrusions, involved the exposure of atoms near the end of a lipid tail, were more likely in curved vesicles or micelles. The same simulations also showed that elbow protrusions occurred on a timescale of approximately 10–100 ns per lipid while splay protrusions appeared on a timescale of 100–1,000 ns depending on the distance threshold.

The potential of mean force for inducing a protrusion was also calculated for a similar set of bilayer systems. The PMFs identified an energy barrier of approximately 8.4 kT to induce a protrusion to the phosphate peak at $d_p = 0.0$ nm, with a slope of 11.1 kT per nm for protruding farther into solution. The origin of this barrier was largely due to water contact and as a result independent of lipid species with the exception of a small decrease in the barrier for unsaturated DOPC and POPC lipid tails. The PMFs also confirmed a slight preference for elbow protrusions at the interface and splay protrusions at increasing distances from the bilayer center. PMFs between bilayers of decreasing water layer thickness were nearly identical until a critical thickness of 0.6 nm was reached at which point bilayer head groups began to interpenetrate and the PMF significantly increased. These results indicate a preferred inter-bilayer separation of approximately 0.8 nm where protrusion contact is most likely, which agrees well with experimental measurements of stalk formation at a critical threshold of 0.9 nm [10]. The increase in the barrier for tail protrusion in highly dehydrated bilayers may also

emphasize the importance of fusion peptides for driving fusion in bilayers that are in close proximity as they can increase protrusion propensity [33,34].

The likelihood of lipid tail protrusions was generally unaffected by lipid type in single- and multi-component bilayers composed of lipids with phosphatidylcholine head groups, and was only observed to decrease when the bilayers were dehydrated to below a critical threshold corresponding to an interbilayer separation of approximately 0.6 nm. Studying protrusion probability in bilayers with high curvature, however, showed conditions under which the protrusion probability could significantly increase. Specifically, protrusion probability in curved vesicles and micelles was observed to increase over planar bilayers by factors of 1.39 and 2.40 respectively. To put these values in context, prior simulations have found that membrane-active fusion peptides may increase protrusion propensity by a factor as large as 4–6× [33,34] while membrane-embedded nanoparticles may increase protrusions locally by a factor of up to 4.2× [63]. The effect of modified properties in protein-free bilayers is less significant; however, it is also possible that these effects are additive in curved bilayers with multiple lipid compositions and perturbing proteins/nanoparticles, and future work will explore this possibility.

The results of this study suggest several avenues for future exploration. The observation of increased protrusion likelihood for curved membranes and a decreased PMF for unsaturated lipids indicates that alternative lipid compositions may have a significant effect. For example, recent work has shown that lipids with negative intrinsic curvature can produce properties similar to the positive curvature exhibited by micelles or vesicles, and thus may increase protrusion probabilities in a similar fashion [39]. Similarly, polyunsaturated lipids may increase protrusion propensity significantly. While we did not observe protrusion probability to substantially increase in mixed bilayers composed of lipids with phosphatidylcholine head groups, it is likely that bilayers containing a mixture of other lipid types and mimicking the true composition of biological membranes may exhibit much larger protrusion probabilities. Similarly, the presence of membrane-active proteins and other molecules may also increase protrusion likelihood. For example, prior simulations have shown that membrane-active fusion peptides may promote lipid tail protrusions by locally disordering lipid tails [34], with a similar increase observed in the vicinity of membrane-embedded nanoparticles [63]. Of particular interest is whether systems with lipid domains, such as lipid rafts, promote protrusions at domain interfaces where the bilayer is locally perturbed. Previous studies have shown that raft boundaries are binding targets for proteins [64,65] which may be related to an enhanced likelihood of protrusion contact in analogy to the protrusion contact that triggers nanoparticle insertion [37]. Finally, it will be important to ascertain whether coarse-grained force fields, such as the MARTINI force field, are able to identify trends in protrusion propensity. Using such coarse-grained approaches will enable the proposed simulations of rafts [66], diverse lipid components [62], and vesicles with mixed lipid compositions [41] that are computationally challenging using atomistic approaches. Future work will directly compare the results of these atomistic simulations to coarse-grained models with the goal of developing improved methods to study protrusion propensity in complex membrane-mimicking systems.

5. Conclusions

In this work, we utilized atomistic molecular dynamics simulations to study the relationship between lipid bilayer composition, curvature, and hydration on the ability of lipid tails to spontaneously protrude into solvent. Previous work has established that these lipid fluctuations play an essential role in biologically ubiquitous processes like membrane fusion, and this work is one of the first efforts to comprehensively profile the dependence of lipid tail protrusions on membrane characteristics. We used unbiased molecular dynamics simulations in

conjunction with potential of mean force calculations to identify elbow and splay protrusions as the dominant modes of lipid tail infiltration of solvent. The potential of mean force for protrusion indicated an energy barrier for collocating lipid tail atoms into the bilayer head group region, and a larger barrier as the hydrophobic lipid tail protruded further and intercalated with the solvent molecules. The PMFs and unbiased simulations indicated that the likelihood for protrusion was relatively insensitive to lipid type in single- and multi-component bilayers composed of lipids with phosphatidylcholine head groups. In contrast, the propensity for tail protrusion was enhanced by the presence of membrane curvature, with increased curvature particularly associated with substantial increase in the incidence of splay mode of protrusion. We also highlighted the role of membrane dehydration below a critical threshold in potentially suppressing the ability of lipid tails to protrude towards solvent, and discussed the implications of this dependence in biological fusion processes.

Additional data and further discussion of simulation methods are available as supplementary information online. Supplementary data associated with this article can be found in the online version, at <http://dx.doi.org/10.1016/j.bbamem.2016.01.026>.

Author contributions

M.A.T., R.C.V.L. and S.H.C. performed simulation work. M.A.T., R.V.C.L., S.H.C., and A.A.K. participated in planning the investigations, analyzing simulation data, and preparing the manuscript. M.A.T and R.C.V.L. contributed equally to this work.

Transparency document

The [transparency document](#) associated with this article can be found, in online version.

Acknowledgements

This work was supported by the MRSEC Program of the National Science Foundation under award number DMR-0819762 and by the NSF CAREER Award No. DMR-1054671. M.A.T. acknowledges support from the Department of Energy through the Computational Science Graduate Fellowship under grant number DE-FG02-97ER25308. The simulations in this work used the Extreme Science and Engineering Discovery Environment (XSEDE), which is supported by National Science Foundation grant number OCI-1053575. Some simulations were run on the Odyssey cluster supported by the FAS Sciences Division Research Computing Group.

References

- [1] D.W. Deamer, J. Bramhall, Permeability of lipid bilayers to water and ionic solutes, *Chem. Phys. Lipids* 40 (1986) 167–188.
- [2] F.R. Maxfield, T.E. McGraw, Endocytic recycling, *Nat. Rev. Mol. Cell Biol.* 5 (2004) 121–132.
- [3] R. Jahn, T.C. Südhof, Membrane fusion and exocytosis, *Annu. Rev. Biochem.* 68 (1999) 863–911.
- [4] Y.A. Chen, R.H. Scheller, SNARE-mediated membrane fusion, *Nat. Rev. Mol. Cell Biol.* 2 (2001) 98–106.
- [5] A. Jeremic, W. Cho, B. Jena, Membrane fusion: what may transpire at the atomic level, *J. Biol. Phys. Chem.* 4 (2004) 139–142.
- [6] W.J. Cho, A. Jeremic, B.P. Jena, Size of supramolecular SNARE complex: membrane-directed self-assembly, *J. Am. Chem. Soc.* 127 (2005) 10156–10157.
- [7] V.S. Malinin, B.R. Lentz, Energetics of vesicle fusion intermediates: comparison of calculations with observed effects of osmotic and curvature stresses, *Biophys. J.* 86 (2004) 2951–2964.
- [8] L.V. Chernomordik, M.M. Kozlov, Mechanics of membrane fusion, *Nat. Struct. Mol. Biol.* 15 (2008) 675–683.
- [9] A. Grafmüller, J. Shillcock, R. Lipowsky, The fusion of membranes and vesicles: pathway and energy barriers from dissipative particle dynamics, *Biophys. J.* 96 (2009) 2658–2675.
- [10] S. Aeffner, T. Reusch, B. Weinhausen, T. Salditt, Energetics of stalk intermediates in membrane fusion are controlled by lipid composition, *Proc. Natl. Acad. Sci. U. S. A.* 109 (2012) E1609–E1618.

- [11] J. Marra, J. Israelachvili, Direct measurements of forces between phosphatidylcholine and phosphatidylethanolamine bilayers in aqueous electrolyte solutions, *Biochemistry* 24 (1985) 4608–4618.
- [12] E. Schneek, F. Sedlmeier, R.R. Netz, Hydration repulsion between biomembranes results from an interplay of dehydration and depolarization, *Proc. Natl. Acad. Sci. USA* 109 (2012) 14405–14409.
- [13] A. Efrat, L.V. Chernomordik, M.M. Kozlov, Point-like protrusion as a prestalk intermediate in membrane fusion pathway, *Biophys. J.* 92 (2007) L61–L63.
- [14] Y. Kozlovsky, M.M. Kozlov, Stalk model of membrane fusion: solution of energy crisis, *Biophys. J.* 82 (2002) 882–895.
- [15] H. Chakraborty, P.K. Tarafdar, M.J. Bruno, T. Sengupta, B.R. Lentz, Activation thermodynamics of poly(ethylene glycol)-mediated model membrane fusion support mechanistic models of stalk and pore formation, *Biophys. J.* 102 (2012) 2751–2760.
- [16] C.K. Haluska, K.A. Riske, V. Marchi-Artzner, J.-M. Lehn, R. Lipowsky, R. Dimova, Time scales of membrane fusion revealed by direct imaging of vesicle fusion with high temporal resolution, *Proc. Natl. Acad. Sci. U. S. A.* 103 (2006) 15841–15846.
- [17] H.J. Risselada, G. Bubnis, H. Grubmüller, Expansion of the fusion stalk and its implication for biological membrane fusion, *Proc. Natl. Acad. Sci. U. S. A.* 111 (2014) 11043–11048.
- [18] J. Nikolaus, M. Stöckl, D. Langosch, R. Volkmer, A. Herrmann, Direct visualization of large and protein-free hemifusion diaphragms, *Biophys. J.* 98 (2010) 1192–1199.
- [19] L.V. Chernomordik, M.M. Kozlov, Protein–lipid interplay in fusion and fission of biological membranes, *Annu. Rev. Biochem.* 72 (2003) 175–207.
- [20] P.M. Kasson, V.S. Pande, Control of membrane fusion mechanism by lipid composition: predictions from ensemble molecular dynamics, *PLoS Comput. Biol.* 3 (2007) e220.
- [21] S. Ohta-lino, M. Pasenkiewicz-Gierula, Y. Takaoka, H. Miyagawa, K. Kitamura, A. Kusumi, Fast lipid disorientation at the onset of membrane fusion revealed by molecular dynamics simulations, *Biophys. J.* 81 (2001) 217–224.
- [22] P.M. Kasson, N.W. Kelley, N. Singhal, M. Vrljic, A.T. Brunger, V.S. Pande, Ensemble molecular dynamics yields submillisecond kinetics and intermediates of membrane fusion, *Proc. Natl. Acad. Sci. U. S. A.* 103 (2006) 11916–11921.
- [23] A.F. Smeijers, A.J. Markvoort, K. Pieterse, P.A.J. Hilbers, A detailed look at vesicle fusion, *J. Phys. Chem. B* 110 (2006) 13212–13219.
- [24] A. Grafmüller, J. Shillcock, R. Lipowsky, Pathway of membrane fusion with two tension-dependent energy barriers, *Phys. Rev. Lett.* 98 (2007) 218101.
- [25] V. Knecht, S.-J. Marrink, Molecular dynamics simulations of lipid vesicle fusion in atomic detail, *Biophys. J.* 92 (2007) 4254–4261.
- [26] A.J. Markvoort, S.J. Marrink, Lipid acrobatics in the membrane fusion arena, *Curr. Top. Membr.* 68 (2011) 259–294.
- [27] K. Yang, Y.-q. Ma, Computer simulations of fusion, fission and shape deformation in lipid membranes, *Soft Matter* 8 (2011) 606–618.
- [28] M. Müller, Y.G. Smirnova, G. Marelli, M. Fuhrmans, A.-C. Shi, Transition path from two apposed membranes to a stalk obtained by a combination of particle simulations and string method, *Phys. Rev. Lett.* 108 (2012) 228103.
- [29] H.J. Risselada, G. Marelli, M. Fuhrmans, Y.G. Smirnova, H. Grubmüller, S.J. Marrink, M. Müller, Line-tension controlled mechanism for influenza fusion, *PLoS ONE* 7 (2012) e38302.
- [30] H.-H.G. Tsai, C.-M. Chang, J.-B. Lee, Multi-step formation of a hemifusion diaphragm for vesicle fusion revealed by all-atom molecular dynamics simulations, *BBA-Biomembr.* 1838 (2014) 1529–1535.
- [31] M.J. Stevens, J.H. Hoh, T.B. Woolf, Insights into the molecular mechanism of membrane fusion from simulation: evidence for the association of splayed tails, *Phys. Rev. Lett.* 91 (2003) 188102.
- [32] D. Mirjanian, A.N. Dickey, J.H. Hoh, T.B. Woolf, M.J. Stevens, Splaying of aliphatic tails plays a central role in barrier crossing during liposome fusion, *J. Phys. Chem. B* 114 (2010) 11061–11068.
- [33] P.M. Kasson, E. Lindahl, V.S. Pande, Atomic-resolution simulations predict a transition state for vesicle fusion defined by contact of a few lipid tails, *PLoS Comput. Biol.* 6 (2010) e1000829.
- [34] P. Larsson, P.M. Kasson, Lipid tail protrusion in simulations predicts fusogenic activity of influenza fusion peptide mutants and conformational models, *PLoS Comput. Biol.* 9 (2013) e1002950.
- [35] S. Kawamoto, W. Shinoda, Free energy analysis along the stalk mechanism of membrane fusion, *Soft Matter* 10 (2014) 3048–3054.
- [36] Y.G. Smirnova, S.-J. Marrink, R. Lipowsky, V. Knecht, Solvent-exposed tails as prestalk transition states for membrane fusion at low hydration, *J. Am. Chem. Soc.* 132 (2010) 6710–6718.
- [37] R.C. Van Lehn, M. Ricci, R.P. Carney, K. Voitchovsky, F. Stellacci, A. Alexander-Katz, Lipid tail protrusions mediate the insertion of nanoparticles into model cell membranes, *Nat. Commun.* 5 (2014) 4482.
- [38] M. Mihailescu, R.G. Vaswani, E. Jardón-Valadez, F. Castro-Román, J.A. Freites, D.L. Worcester, A.R. Chamberlin, D.J. Tobias, S.H. White, Acyl-chain methyl distributions of liquid-ordered and disordered membranes, *Biophysical Journal* 100 (2011) 1455–1462.
- [39] L. Vamparys, R. Gautier, S. Vanni, W.F.D. Bennett, D.P. Tieleman, B. Antonny, C. Etchebest, P.J. Fuchs, Conical lipids in flat bilayers induce packing defects similar to that induced by positive curvature, *Biophys. J.* 104 (2013) 585–593.
- [40] M. Pinot, S. Vanni, S. Pagnotta, S. Lacas-Gervais, L.-A. Payet, T. Ferreira, R. Gautier, B. Goud, B. Antonny, H. Barelli, Polyunsaturated phospholipids facilitate membrane deformation and fission by endocytic proteins, *Science* 345 (2014) 693–697.
- [41] S. Vanni, H. Hirose, H. Barelli, B. Antonny, R. Gautier, A sub-nanometre view of how membrane curvature and composition modulate lipid packing and protein recruitment, *Nat. Commun.* 5 (2014) 4916.
- [42] N. Sapay, W.F.D. Bennett, D.P. Tieleman, Thermodynamics of flip-flop and desorption for a systematic series of phosphatidylcholine lipids, *Soft Matter* 5 (2009) 3295–3302.
- [43] A. Grafmüller, R. Lipowsky, V. Knecht, Effect of tension and curvature on the chemical potential of lipids in lipid aggregates, *Phys. Chem. Chem. Phys.* 15 (2013) 876–881.
- [44] D. Poger, A.E. Mark, On the validation of molecular dynamics simulations of saturated and cis-monounsaturated phosphatidylcholine lipid bilayers: a comparison with experiment, *J. Chem. Theory Comput.* 6 (2010) 325–336.
- [45] T.A. Wassenaar, K. Pluhackova, R.A. Böckmann, S.J. Marrink, D.P. Tieleman, Going backward: a flexible geometric approach to reverse transformation from coarse grained to atomistic models, *J. Chem. Theory Comput.* 10 (2014) 676–690.
- [46] S.J. Marrink, H.J. Risselada, S. Yefimov, D.P. Tieleman, A.H. de Vries, The MARTINI force field: coarse grained model for biomolecular simulations, *J. Phys. Chem. B* 111 (2007) 7812–7824.
- [47] D. Poger, W.F. Van Gunsteren, A.E. Mark, A new force field for simulating phosphatidylcholine bilayers, *J. Comput. Chem.* 31 (2010) 1117–1125.
- [48] N. Schmid, A.P. Eichenberger, A. Choutko, S. Riniker, M. Winger, A.E. Mark, W.F. van Gunsteren, Definition and testing of the GROMOS force-field versions 54 A7 and 54B7, *Eur. Biophys. J.* 40 (2011) 843–856.
- [49] B. Hess, P.-LINCOS: a parallel linear constraint solver for molecular simulation, *J. Chem. Theory Comput.* 4 (2008) 116–122.
- [50] D. Poger, A.E. Mark, Lipid bilayers: the effect of force field on ordering and dynamics, *J. Chem. Theory Comput.* 8 (2012) 4807–4817.
- [51] B. Hess, C. Kutzner, D. van der Spoel, E. Lindahl, GROMACS 4: algorithms for highly efficient, load-balanced, and scalable molecular simulation, *J. Chem. Theory Comput.* 4 (2008) 435–447.
- [52] W. Humphrey, A. Dalke, K. Schulten, VMD: visual molecular dynamics, *J. Mol. Graphics* 14 (1996) 33–38.
- [53] S. Kumar, J.M. Rosenberg, D. Bouzida, R.H. Swendsen, P.A. Kollman, The weighted histogram analysis method for free-energy calculations on biomolecules. i. the method, *J. Comput. Chem.* 13 (1992) 1011–1021.
- [54] B. Roux, The calculation of the potential of mean force using computer simulations, *Comp. Phys. Comm.* 91 (1995) 275–282.
- [55] J.S. Hub, B.L. de Groot, D. van der Spoel, g_wham: free weighted histogram analysis implementation including robust error and autocorrelation estimates, *J. Chem. Theory Comput.* 6 (2010) 3713–3720.
- [56] H. Cui, E. Lyman, G.A. Voth, Mechanism of membrane curvature sensing by amphipathic helix containing proteins, *Biophys. J.* 100 (2011) 1271–1279.
- [57] K. Rajamoorthi, H.I. Petrache, T.J. McIntosh, M.F. Brown, Packing and viscoelasticity of polyunsaturated omega-3 and omega-6 lipid bilayers as seen by (2)H NMR and X-ray diffraction, *J. Am. Chem. Soc.* 127 (2005) 1576–1588.
- [58] R.J. Mashl, H.L. Scott, S. Subramaniam, E. Jakobsson, Molecular simulation of dioleoylphosphatidylcholine lipid bilayers at differing levels of hydration, *Biophys. J.* 81 (2001) 3005–3015.
- [59] E.A. Golovina, A.V. Golovin, F.A. Hoekstra, R. Faller, Water replacement hypothesis in atomic detail—factors determining the structure of dehydrated bilayer stacks, *Biophys. J.* 97 (2009) 490–499.
- [60] S. Pronk, E. Lindahl, P.M. Kasson, Coupled diffusion in lipid bilayers upon close approach, *J. Am. Chem. Soc.* (2014) <http://dx.doi.org/10.1021/ja508803d> (in press).
- [61] H.J. Risselada, S.J. Marrink, Curvature effects on lipid packing and dynamics in liposomes revealed by coarse grained molecular dynamics simulations, *Phys. Chem. Chem. Phys.* 11 (2009) 2056–2067.
- [62] H.I. Ingólfsson, M.N. Melo, F.J. van Eerden, C. Amarez, C.A. Lopez, T.A. Wassenaar, X. Periole, A.H. de Vries, D.P. Tieleman, S.J. Marrink, Lipid organization of the plasma membrane, *J. Am. Chem. Soc.* 136 (2014) 14554–14559.
- [63] R.C. Van Lehn, A. Alexander-Katz, Membrane-embedded nanoparticles induce lipid rearrangements similar to those exhibited by biological membrane proteins, *J. Phys. Chem. B* 118 (2014) 12586–12598.
- [64] C. Nicolini, J. Baranski, S. Schlummer, J. Palomo, M. Lumbierres-Burgues, M. Kahms, J. Kuhlmann, S. Sanchez, E. Gratton, H. Waldmann, R. Winter, Visualizing association of N-ras in lipid microdomains: influence of domain structure and interfacial adsorption, *J. Am. Chem. Soc.* 128 (2006) 192–201.
- [65] P. Schön, A.J. García-Sáez, P. Malovrh, K. Bacia, G. Anderluh, P. Schwille, Equinatoxin II permeabilizing activity depends on the presence of sphingomyelin and lipid phase coexistence, *Biophys. J.* 95 (2008) 691–698.
- [66] H.J. Risselada, S.J. Marrink, The molecular force of lipid rafts in model membranes, *Proc. Natl. Acad. Sci. USA* 105 (2008) 17367–17372.

Supporting information for:

Solvent-exposed lipid tail protrusions depend on lipid membrane composition and curvature

Mukarram A. Tahir*, Reid C. Van Lehn*, Sang Hyun Choi, and Alfredo Alexander-Katz*

*Department of Materials Science and Engineering, Massachusetts Institute of Technology,
Cambridge, MA, USA*

E-mail: aalexand@mit.edu

Summary of simulation systems

Bilayers of different compositions, hydration, and curvature were prepared and simulated to model the effect of various factors on protrusion likelihood. Table S1 summarizes the physical properties of each of these bilayers while Table S2 summarizes relevant simulation quantities. In Table S1, the area per lipid for each bilayer was estimated from the average area of the simulation box divided by the number of lipids in each monolayer. This value is omitted for the curved micelle/vesicle. The bilayer thickness was computed as the distance between phosphate peaks from electron density plots similar to those shown in Figure 4 of the main text and Figure S5. All experimental melting points are reproduced from the Avanti website.^{S1} The radii of the micelle/vesicle were estimated from the phosphate peak of the electron density plots calculated radially from the bilayer center of mass (data not shown), with the radius of the vesicle approximated as the distance to the farther phosphate peak

corresponding to the vesicle’s outer bilayer. In Table S2, equilibration times are reported for initial simulation with a Berendsen (abbreviated B) barostat followed by a second simulation with a Parrinello-Rahman (abbreviated PR) barostat as described in the main text. The number of simulations refers to the number of times each prepared bilayer was separately equilibrated and run from different initialized velocities. The number of US windows was determined from the thickness of the bilayers shown in Table S1.

Mixed bilayer simulation details

Mixed bilayers consisting of 512 lipids in a 1:1 ratio of either DPPC:DOPC or DPPC:DLPC, and single-component DOPC, DLPC, and DPPC bilayers with 512 lipids, were created using the `insane.py` Python script available from the MARTINI website.^{S2} Initial bilayers were assembled using v2.1 of the MARTINI force field which coarse-grains approximately 4 heavy atoms to 1 coarse-grained bead.^{S3} The 4-to-1 mapping greatly reduces the simulation size and allows the use of a larger timestep in order to more rapidly achieve the long times necessary to observe lipid mixing. The mixed bilayers were each equilibrated for 3 μ s using a simulation timestep of 30 fs. Non-bonded interactions were calculated using a shifted Lennard-Jones potential with a cutoff of 1.2 nm and with the shift applied after 0.9 nm for dispersion interactions. The standard unpolarized MARTINI water model was used, so the system dielectric constant was set to 15 to screen electrostatic interactions and account for missing water charges. The neighbor list was updated every 300 fs with a cutoff of 1.4 nm. Constant temperature was maintained at 323 K using a velocity-rescale thermostat with a time constant of 1.0 ps. Constant pressure was maintained at 1.0 bar using a Berendsen barostat with a time constant of 12.0 ps and a isothermal compressibility of 3×10^{-4} bar⁻¹. After equilibration, the MARTINI lipids were reverse coarse-grained back to atomistic resolution using the recently developed `backwards.py` script^{S4} followed by additional equilibration at atomistic resolution (Table S2). Figure S2 summarizes system preparation

and shows snapshots of both the coarse-grained and atomistic systems.

Curved bilayer simulation details

Like the mixed bilayers, both the micelle and vesicle systems were prepared using a reverse coarse-graining procedure using the MARTINI force field. The micelle was assembled by randomly distributing 50 DOPC lipids in a rhombic dodecahedral simulation box with an excess of solvent (20,633 coarse-grained water beads) and simulating for 300 ns using the parameters described above. Self-assembly occurred within the first 50 ns. At the end of 300 ns, excess water was removed and the system was reverse coarse-grained using the backwards.py script.^{S4} The vesicle was assembled by first positioning 900 lipids in a rhombic dodecahedral simulation box using the martini-vesicle-builder.py script available from the MARTINI website.^{S5} The outer bilayer consisted of 646 lipids while the inner bilayer contained 254. The vesicle was then equilibrated for 500 ns and reverse coarse-grained. Both systems were again equilibrated briefly after reverse coarse-graining (Table S2). Figure S2 summarizes the vesicle preparation.

In planar bilayers, d_p was calculated as the distance between a tail atom and the same lipid's phosphorus atom projected along the membrane normal (i.e. the z-axis). However, this definition is inadequate to describe protrusions in curved bilayers, as the membrane normal varies locally across the bilayer surface and the distance to the same lipid's phosphorus atom may not model protrusion into solution. As a result, an alternative definition was used to account for these two factors. First, the membrane normal was approximated as a vector from each lipid's phosphorus atom to the center of mass of all water molecules within 1.5 nm. This approach is accurate due to the asymmetric distribution of water molecules which are excluded from the hydrophobic bilayer core. The normal was calculated for each lipid for each timestep. Protrusions were identified by calculating the distance between each hydrophobic tail atom and the nearest phosphorus atom projected along that phosphorus

atom's normal. Figure S3 illustrates this method for an example splay protrusion in the lipid vesicle with the water molecules used to determine the membrane normal drawn explicitly. This method predicted slightly different values for the average number of protrusions in planar bilayers than the method that identified protrusions by comparing to the same lipid's phosphorus atom. However, the same trends in the frequency of protrusions for different tail atoms and changes in the average number of protrusions for different threshold values of d_p were identified, confirming the suitability of using this method to predict trends in protrusion likelihood as a function of curvature.

PMF calculation for fully-hydrated bilayers

In the main text, the potential of mean force (PMF) for inducing a lipid protrusion is shown for several different bilayer compositions and levels of hydration. The PMF was calculated using umbrella sampling simulations. For fully-hydrated single-component bilayers, two lipid protrusions were induced by pulling on atoms in both monolayers simultaneously to increase sampling without additional computational expense. A similar method has been used previously in the study of lipid flip-flop and lipid desorption.^{S6,S7} The two lipids were chosen to be spaced apart by at least 3 nm in-plane to diminish any possible lipid-lipid interactions. Finally, to minimize the overall bilayer disruption, the two atoms were pulled to different positions such that sum of the distances to which both beads were pulled was a constant. Figure S4 illustrates this pulling workflow with the two constrained tail beads drawn in red. Figure S6 shows the convergence of the two PMFs (i.e. for lipids in the upper/lower leaflets) for a DPPC bilayer. Both PMFs converge within the 70 ns sampling interval and nearly identical profiles are obtained for both leaflets as expected.

Dehydrated bilayer simulation details

DOPC bilayers were modeled at varying levels of hydration and corresponding water layer thicknesses between bilayers, D_w . Two different methods were used to model dehydration as shown in Fig. S5. For unbiased simulations, the bilayer was modeled using the same techniques as in the main text with the level of hydration modified accordingly. Fig. S5a-c show snapshots of bilayers with hydrations of 5, 10, and 25 water molecules/lipid with electron density plots for each showing the distribution of system components. D_w was estimated as the distance between the phosphate peaks through the water region as indicated. Note that two distinct choline peaks are no longer observed for a hydration level of 5 water molecules/lipid, indicating strong interpenetration of head groups between the two bilayer leaflets as is also apparent in the simulation snapshot. Fig. S9f summarizes the unbiased protrusion calculations at different levels of hydration. The small box size for bilayers at low hydration prevented umbrella sampling simulations from being correctly run due to the need to enforce distance restraints in excess of half the box z-vector. To solve this problem, a double bilayer setup was constructed where the same bilayer from the single-bilayer simulations was duplicated in the z-position to double the box size. PMFs were then computed by pulling lipids toward the central water layer as illustrated in Fig. S5d. All simulations were conducted at 300 K with 64 lipids per bilayer (128 lipids total in double bilayer simulations) as summarized in Table S2.

Additional unbiased simulation results

In the main text, the time-averaged number of protrusions per lipid was reported for a series of single-component bilayers from unbiased simulations (Figure 2). As shown in Figure S7, a time-averaging over a sampling time of 200 ns was sufficient for convergence of these protrusion frequencies. In addition, two lipid protrusion modes were identified as shown for DOPC (Figure 3). Both splay and elbow protrusions were also observed for each other lipid

type from the same unbiased simulations. Figure S8 shows the fraction of total protrusions for each lipid studied as a function of the bead ID in the chain (labeled in Figure S1). The dashed line in each plot indicates the division between elbow/splay protrusion modes used to categorize individual protrusion frequencies below. The protrusion threshold, d_p , was set to 0.1 nm in all plots. The average number of protrusions subdivided into the elbow and splay components is shown in Figure S9a/b. In general elbow protrusions represent approximately 90% of all protrusion events, reflecting the close positioning of these acyl groups to the water interface. No clear trend emerges in the relative likelihood of either protrusion type as previously noted for overall protrusion appearance in the main text.

In addition to the average number of protrusions per lipid, the actual frequency of protrusion occurrence can be approximated from the simulations. The frequency is shown in units of protrusions per lipid per ns in Figure S9c, with Figure S9d and e splitting the overall frequency into elbow and splay components. To calculate the frequency as opposed to the average number of protrusions, only new protrusions were counted in any given simulation timestep by disregarding lipids protruding in the previous timestep. The measured frequency may also be dependent on sampling time due to the time-normalization (as opposed to normalizing by the number of simulation snapshots as with the average number of protrusions); the simulation trajectories used here were sampled every 20 ps. From these results, the typical timescale for a elbow protrusion was 10-100 ns depending on d_p , while the timescale for a splay protrusion was 100-1,000 ns. As expected, the same trends observed for the average number of protrusions are maintained in the protrusion frequency, with splay protrusions occurring approximately an order magnitude less frequently than elbow protrusions but with no clear dependence on bilayer properties.

Finally, the average number of protrusions were also calculated as a function of hydration in Figure S9f to compare with the PMFs in Figure 7 of the main text. Protrusion occurrence was calculated from a total of 6 independent 200 ns trajectories to increase sampling. Compared to the fully hydrated bilayer (60 waters/lipid), the average number of protrusions

was relatively unchanged until a hydration of 5 waters/lipid was reached at which point the likelihood of observing a protrusion dropped significantly. This qualitatively agrees with the PMF results and confirms that poorly dehydrated bilayers are less likely to have protrusions.

Table S1: Summary of systems: physical properties

Lipid type	Lipids	Water molecules	Temp. [K]	Melting temp. [K]	Area per lipid [nm ²]	Thickness [nm]	Radius [nm]
Single-component bilayers							
DLPC	64	3,983	323	271	0.659	2.84	N/A
DMPC	64	3,650	323	297	0.655	3.19	N/A
DPPC	64	3,849	323	314	0.633	3.45	N/A
POPC	64	3,443	323	271	0.654	3.69	N/A
DOPC	64	3,959	323	256	0.676	3.64	N/A
DOPC	64	3,959	300	256	0.674	3.66	N/A
DOPC	512	28,352	323	256	0.672	3.67	N/A
DLPC	512	32,448	323	271	0.651	2.85	N/A
DPPC	512	30,400	323	314	0.635	3.64	N/A
Single bilayer, varying hydrations							
DOPC	64	320	300	256	0.649	3.83	N/A
DOPC	64	448	300	256	0.646	3.78	N/A
DOPC	64	642	300	256	0.650	3.86	N/A
DOPC	64	1,604	300	256	0.659	3.75	N/A
Double bilayers, varying hydration							
DOPC	128	640	300	256	0.656	3.88	N/A
DOPC	128	896	300	256	0.647	3.82	N/A
DOPC	128	1,284	300	256	0.651	3.75	N/A
DOPC	128	3,208	300	256	0.656	3.67	N/A
Mixed lipid compositions							
DPPC/DOPC	512	29,376	323	314/256	0.659	3.65	N/A
DPPC/DLPC	512	31,424	323	314/271	0.649	3.24	N/A
Curved DOPC systems							
Micelle	50	11,818	300	256	N/A	N/A	2.50
Vesicle	900	95,176	300	256	N/A	3.44	6.64

Table S2: Summary of systems: simulation parameters

Lipid type	Lipids	Water molecules	Total atoms	Equil. time (B/PR) [ns]	Run time (PR) [ns]	Num. sims.	US windows
Single-component bilayers							
DLPC	64	3,983	14,637	20/100	200	2	20
DMPC	64	3,650	13,894	20/100	200	2	23
DPPC	64	3,849	14,747	20/100	200	2	26
POPC	64	3,443	13,657	20/100	200	2	26
DOPC	64	3,959	15,333	20/100	200	2	26
DOPC (323K)	64	3,959	15,333	20/100	200	2	26
DOPC	512	28,352	112,704	20/100	200	2	N/A
DLPC	512	32,448	118,848	20/100	200	2	N/A
DPPC	512	30,400	116,800	20/100	200	2	N/A
Single bilayer, varying hydrations							
DOPC	64	320	4,416	20/200	200	6	N/A
DOPC	64	448	4,800	20/200	200	6	N/A
DOPC	64	642	5,382	20/200	200	6	N/A
DOPC	64	1,604	8,268	20/200	200	6	N/A
Double bilayers, varying hydration							
DOPC	128	640	8,832	20/100	N/A	2	26
DOPC	128	896	9,600	20/100	N/A	2	26
DOPC	128	1,284	10,764	20/100	N/A	2	26
DOPC	128	3,208	16,536	20/100	N/A	2	26
Mixed lipid compositions							
DPPC/DOPC	512	29,376	114,752	20/100	200	2	N/A
DPPC/DLPC	512	31,424	117,824	20/100	200	2	N/A
Curved DOPC systems							
Micelle	50	11,818	38,154	1/50	200	2	N/A
Vesicle	900	95,176	334,128	1/20	50	2	N/A

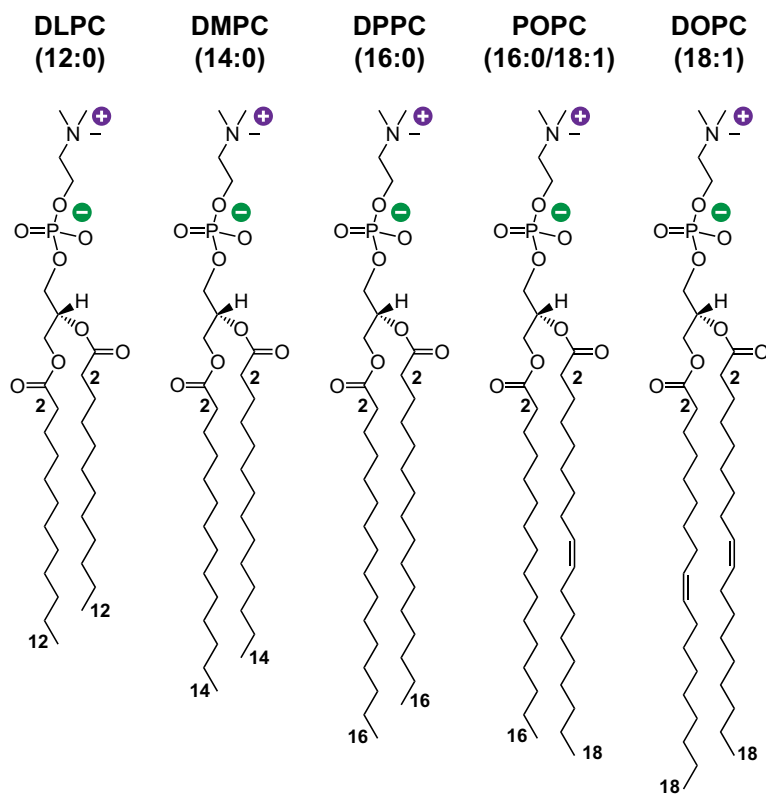


Figure S1: Chemical structures of the five different lipids studied in the main text, labeled both by conventional abbreviation and ratio of single:double bonds in hydrophobic tails.

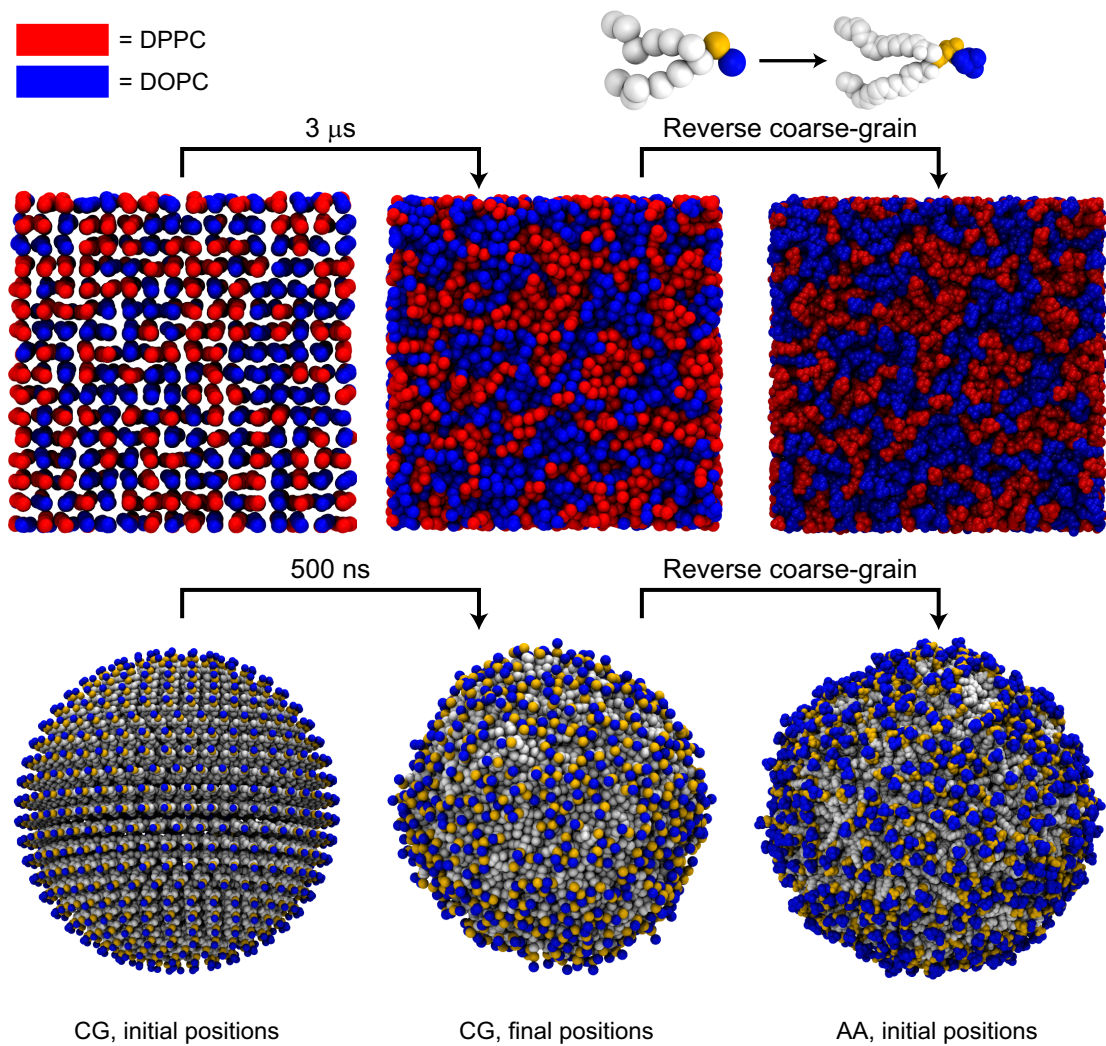


Figure S2: Preparation of mixed bilayers using MARTINI coarse-grained model. Lipids were added in a 1:1 ratio to create a 512 lipid bilayer, equilibrated for $3 \mu\text{s}$ using the coarse-grained force field, then reverse coarse-grained back to the atomistic force field. A vesicle was made in a similar procedure with 500 ns of equilibration prior to reverse coarse-graining. Water is omitted from the simulation snapshots.

Normal vector, pointed into surrounding water from nearest phosphorus atom

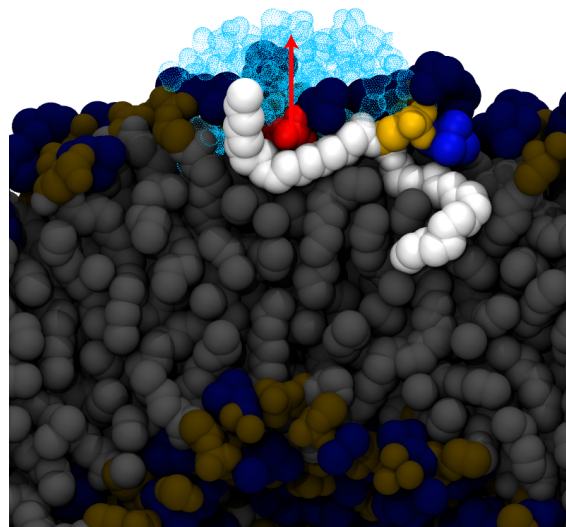


Figure S3: Method for identifying protrusions in curved bilayers with locally-varying membrane normal vectors. For each lipid, a vector is drawn from the head group phosphorus atom to the center of mass of water molecules within 1.5 nm. Protrusions are identified by calculating the distance between a hydrophobic atom and the nearest phosphorus atom, projected along that phosphorus atom's membrane normal. An example splay protrusion identified using this method is identified. The water molecules are drawn in cyan with the nearest phosphate group and corresponding normal vector in red.

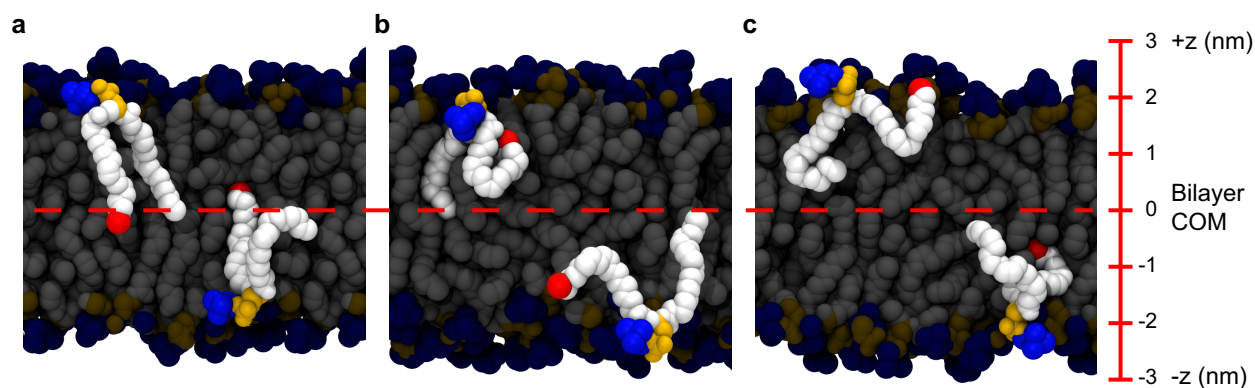


Figure S4: Simulation snapshots illustrating umbrella sampling workflow for a DOPC bilayer. Single atoms in two lipids in opposite monolayers are restrained simultaneously. The restrained atoms are shown in red; the remainder of each lipid is highlighted. The dashed line indicates the center of mass of the bilayer and distances along the z -axis are indicated. **a** Equilibrated bilayer with no restraints on target atoms. **b** Top lipid atom pulled to 1.3 nm, bottom to 1.2 nm. **c** Top lipid pulled to 2.0 nm, bottom to 0.5 nm.

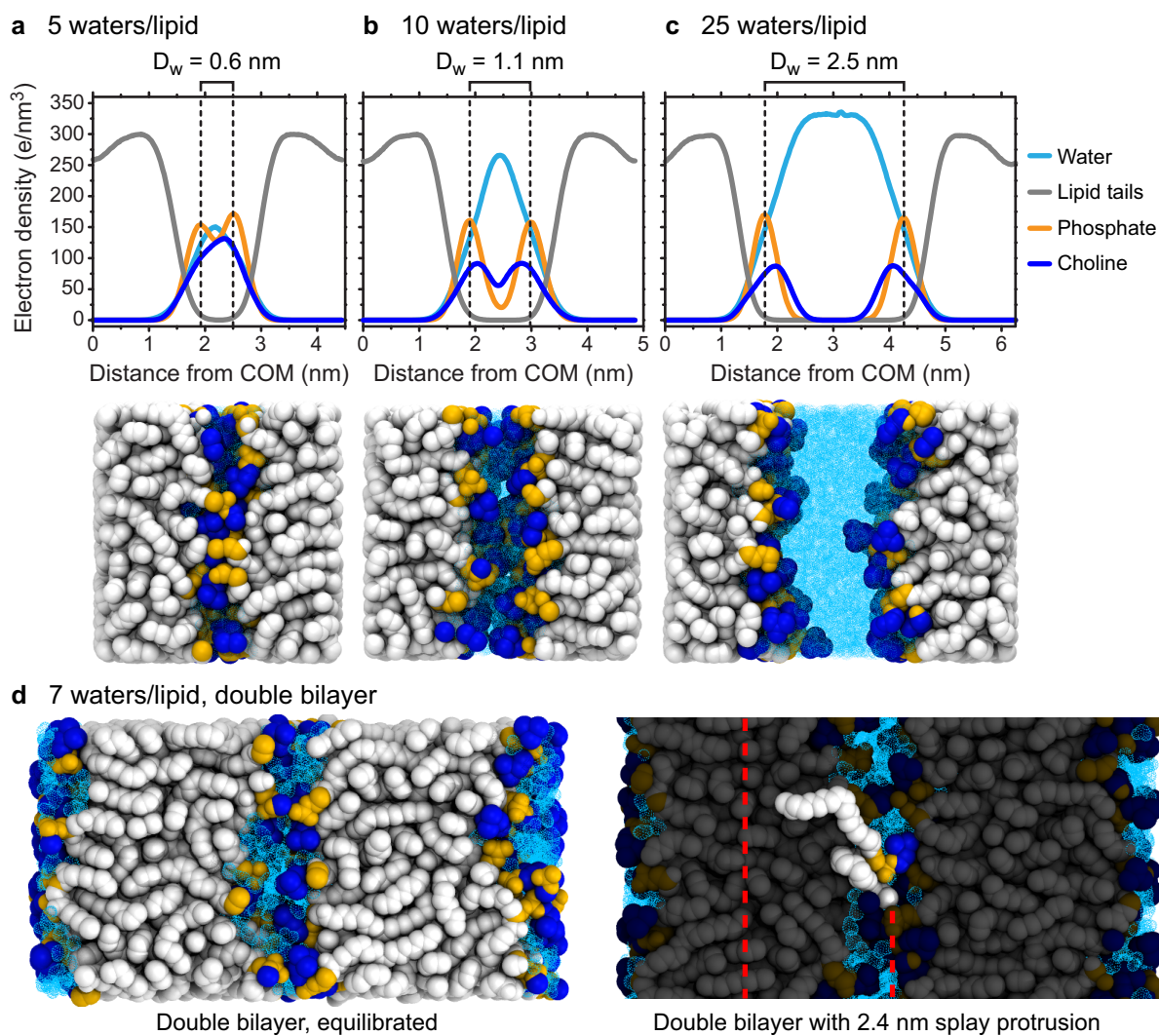


Figure S5: Construction of dehydrated bilayers. Electron densities show the distribution of components and the calculation of the water layer thickness, D_w , for hydration levels of: **a** 5 water molecules/lipid, **b** 10 water molecules/lipid, and **c** 25 water molecules/lipid. **d** Illustration of double bilayer system and induced splay protrusion used in umbrella sampling simulations.

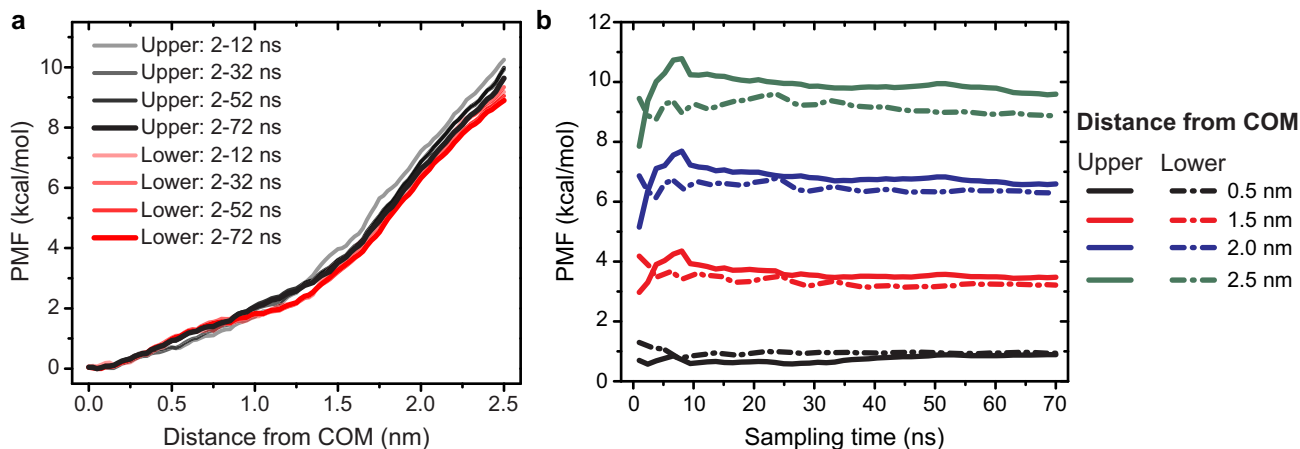


Figure S6: Convergence of PMF for the DPPC bilayer at 323 K. Black and red lines in (a) denote the lipid pulled in the upper and lower leaflet of the bilayer respectively, with darker lines indicating longer intervals. In (b), the PMF is plotted as a function of umbrella sampling duration for various pull distances to demonstrate convergence within 70 ns.

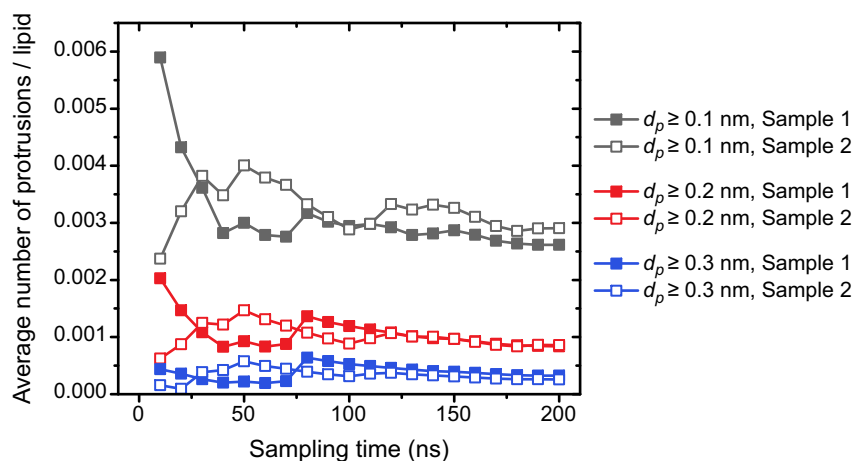


Figure S7: Convergence of protrusion frequency for DOPC bilayer at 323 K. The plot shows protrusion frequency averaged over increasing amounts of time from the unbiased production trajectory. The average number of protrusions per lipid plateaus before 200 ns; the last point (at 200 ns) corresponds to the values shown in the bar charts in the main text. Black, red, and blue lines respectively denote protrusion classification thresholds of $d_p = 0.1$ nm, $d_p = 0.2$ nm, and $d_p = 0.3$ nm, and the plots for two different samples are shown separately.

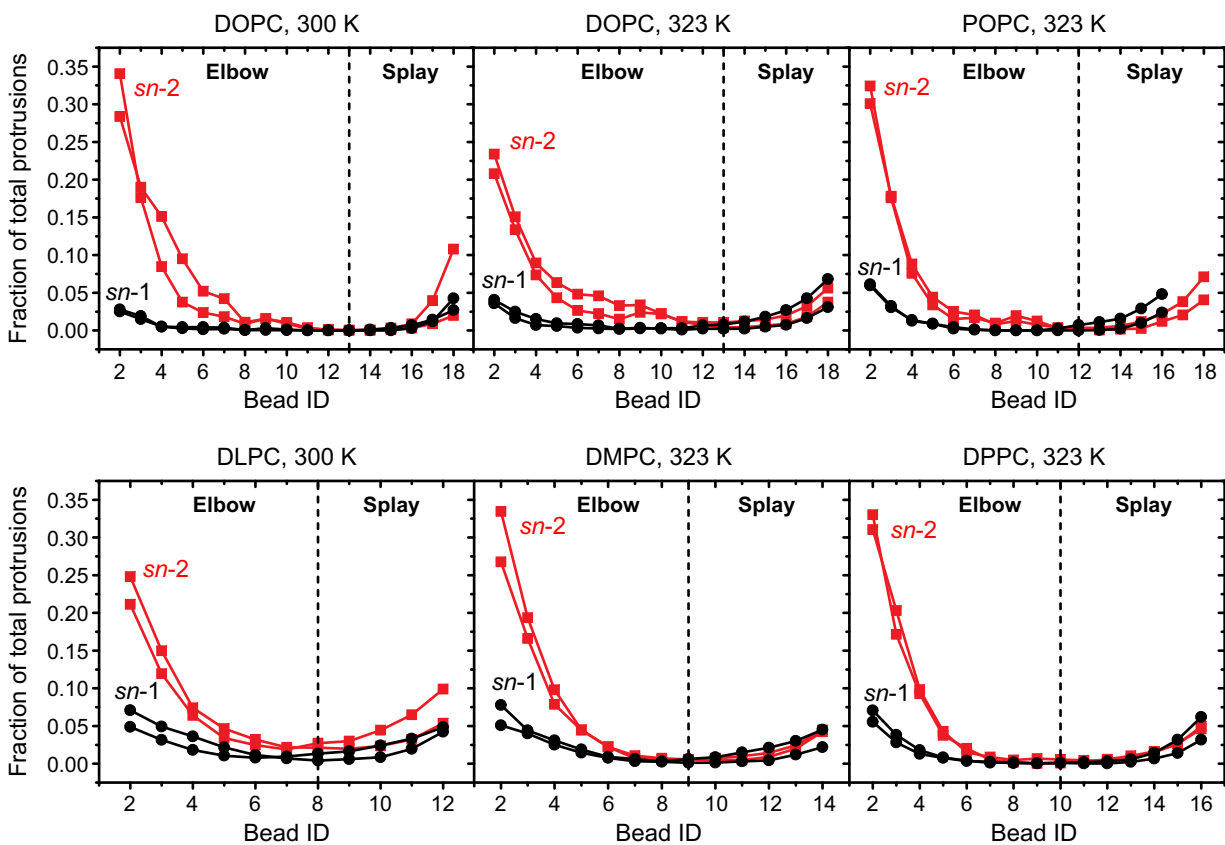


Figure S8: Fraction of total protrusions by bead ID (see Fig. S1) for all systems simulated with $d_p \geq 0.1$ nm. Elbow vs. splay protrusions are differentiated by the regions divided by a vertical dashed line as in Fig. 3 of the main text. Similar trends are observed for all lipids studied.

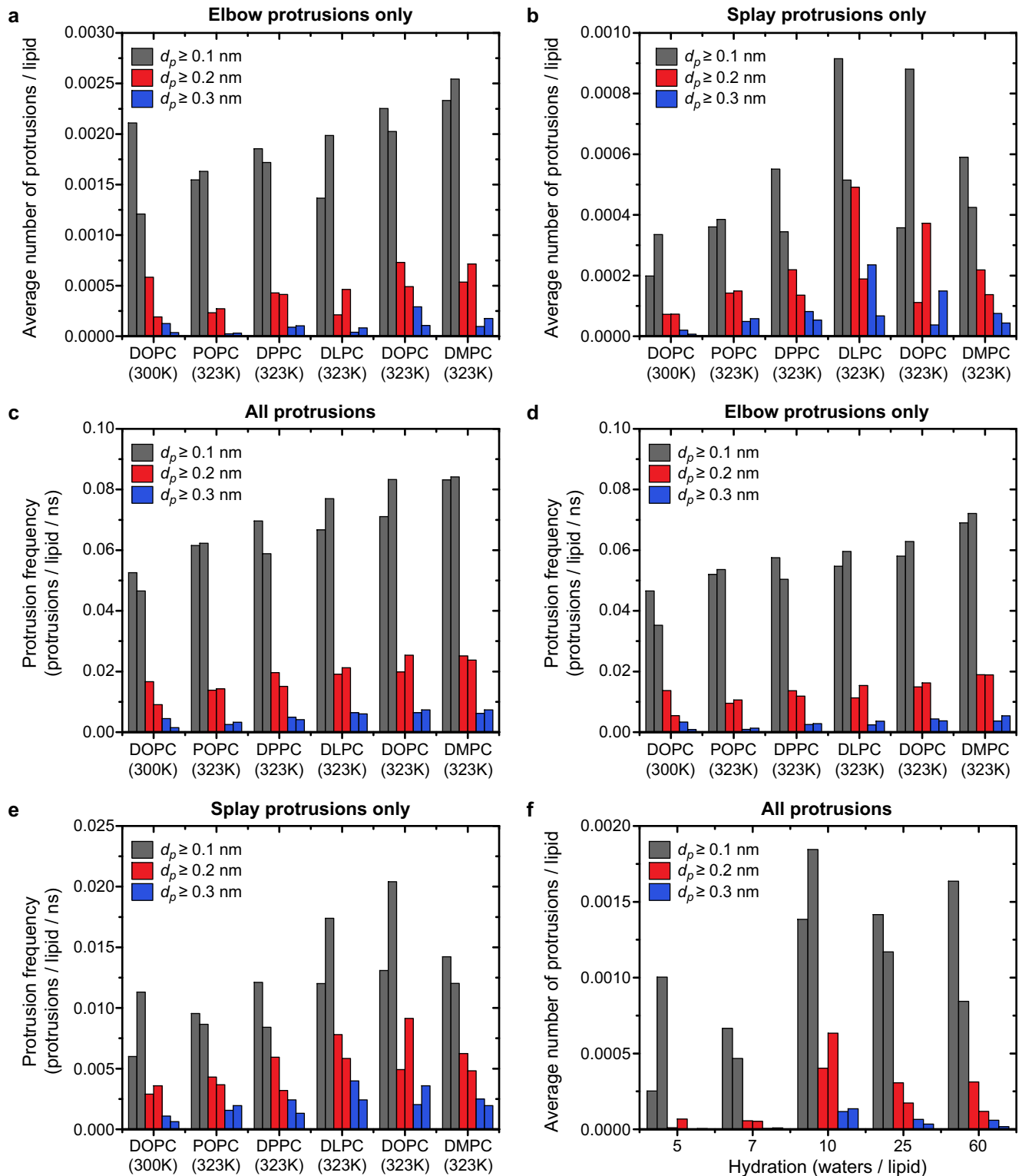


Figure S9: Unbiased protrusion analysis. Average number of elbow (a) and splay (b) protrusions per lipid for each bilayer type. Overall frequency of protrusion appearance for each bilayer (c), split into elbow (d) and splay (e) contributions. f The average number of protrusions as a function of hydration.

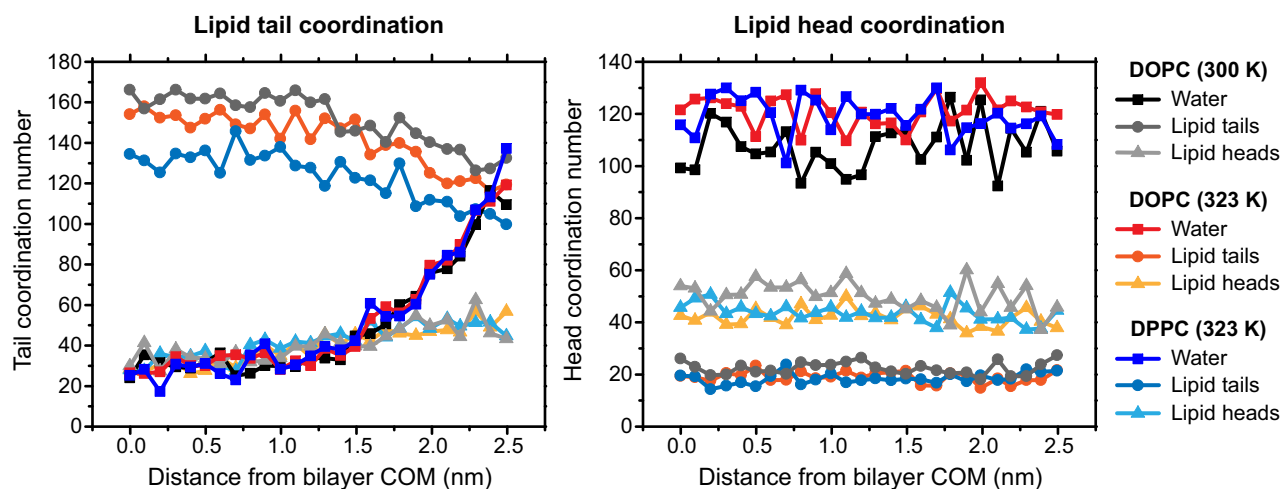


Figure S10: Coordination numbers of lipid head and tail groups for varying lipid species. The coordination number is calculated as the average number of atoms of the given type within 0.6 nm of an atom in the lipid tail (left) or head (right). All coordination numbers were determined from the umbrella sampling simulations as a function of the distance of the pulled atom from the bilayer center of mass (see Fig. S4). Three lipid simulations were considered - DOPC at both 300 and 323 K and DPPC at 323 K. As a protrusion is induced, coordination by water increases significantly for all three lipids while coordination by other tails decreases, consistent with a protrusion entering the solvent region. In contrast, minimal change in head coordination is observed.

References

- (S1) Silvius, J. *Thermotropic Phase Transitions of Pure Lipids in Model Membranes and Their Modifications by Membrane Proteins*; John Wiley & Sons, New York, 1982.
- (S2) Downloaded from: <http://md.chem.rug.nl/cgmartini/images/tools/insane/insane.py>.
- (S3) Marrink, S. J.; Risselada, H. J.; Yefimov, S.; Tieleman, D. P.; de Vries, A. H. The MARTINI force field: coarse grained model for biomolecular simulations. *J. Phys. Chem. B* **2007**, *111*, 7812–7824.
- (S4) Wassenaar, T. A.; Pluhackova, K.; Böckmann, R. A.; Marrink, S. J.; Tieleman, D. P. Going backward: a flexible geometric approach to reverse transformation from coarse grained to atomistic models. *J. Chem. Theory Comput.* **2014**, *10*, 676–690.
- (S5) Downloaded from:
http://md.chem.rug.nl/cgmartini/images/tools/vesicle/martini-vesicle_builder.py.
- (S6) Tieleman, D. P.; Marrink, S.-J. Lipids out of equilibrium: energetics of desorption and pore mediated flip-flop. *J. Am. Chem. Soc.* **2006**, *128*, 12462–12467.
- (S7) Sapay, N.; Bennett, W. F. D.; Tieleman, D. P. Thermodynamics of flip-flop and desorption for a systematic series of phosphatidylcholine lipids. *Soft Matter* **2009**, *5*, 3295–3302.